St Aloysius Prakashana

ISBN-978-81-963171-6-4

Proceedings of the National Conference on
Energy Harvesting Technologies: Tapping the Power of Nature

Editor: Emmanuel Deepak Dsilva

Proceedings of the National Conference on

Energy Harvesting Technologies: Tapping the Power of Nature

organized by Post graduate departments of
Physics and Mathematics
St Aloysius (Deemed to Be University), Mangaluru

in collaboration with
Association of Physics Teachers of
Mangalore University

Sponsored by

Science and Engineering Research Board(SERB)
Department of Science and Technology (DST)
Govt. of India

Supported by

Mangalore Refinery and Petrochemicals Limited

23-24, July 2024

Proceeding of National Conference on Energy Harvesting Technologies: Tapping the Power of Nature

Emmanuel Deepak Dsilva (Editor)

Published by	:	**St Aloysius Prakashana** St Aloysius (Deemed to be University) Kodialbail, P. B. No. 720 Mangaluru - 575 003 Karnataka, India Email: aloyprakashana@staloysius.edu.in
©	:	Author
First Impression	:	2024
Copies	:	100
Pages	:	76+xxx
Paper Used	:	80 GSM
Size	:	1/8 Demy
Price	:	₹ 150.00
ISBN	:	978-81-963171-6-4
Printed by	:	**Meldream Graphics**, Kulshekar, Mangaluru Mob: 9164444069

Please note:

The Authors of the papers and they alone are responsible for the technical content and for the references cited or otherwise in their respective papers.

Message from the Vice Chancellor

It is with great pride and pleasure that I present the proceedings of the National Conference on Energy Harvesting Technologies: Tapping the Power of Nature (EHT-TPN 2024), held from July 23-24, 2024. This conference has been a remarkable event, successfully bringing together a diverse group of experts and scholars to explore and discuss the latest advancements in energy harvesting technologies.

I would like to extend my heartfelt congratulations to the Postgraduate Departments of Physics and Mathematics for their meticulous planning and execution of this conference. Their dedication ensured that the event ran smoothly and exceeded expectations in every aspect.

I also wish to express my deepest gratitude to the sponsors of this National Conference: The Science and Engineering Research Board (SERB), the Department of Science and Technology (DST), and Mangalore Refinery and Petrochemicals Limited (MRPL). Their generous support was instrumental in making this conference a success.

It is particularly noteworthy that we had the privilege of hosting seven esteemed invited speakers, who delivered a total of eight insightful lectures. Additionally, there were ten plenary talks and sixteen poster presentations, all of which significantly contributed to the richness of the conference. I am deeply thankful to each speaker and presenter for their invaluable contributions.

The scope of this conference was impressively diverse, with participants from various fields of research, all united by a common goal: advancing environmentally friendly energy harvesting technologies. The interdisciplinary nature of this event allowed for a broad exchange of ideas and fostered collaborations that will undoubtedly push the boundaries of current research.

individual research but also drive collective progress in the field of energy harvesting.

The proceedings of this conference contain a collection of excellent papers that reflect the innovative thinking and rigorous research of our participants. These papers cover a wide array of topics, extending beyond fundamental physics to include engineering and applied physics. I extend my sincere gratitude to all the authors who contributed to the "Proceedings of the National Conference on Energy Harvesting Technologies: Tapping the Power of Nature."

In conclusion, I would like to express my deepest appreciation to the advisory board members, organizing committee, and all those who played a role in making EHT-TPN 2024 a success. Your unwavering commitment and contributions were the foundation of this event's success. Without your efforts, this conference would not have been possible.

Rev. Dr Praveen Martis SJ
Vice Chancellor
St Aloysius (Deemed to be University)
Mangaluru

Foreword

I write this foreword with great satisfaction and pride. The National Conference on Energy Harvesting Technologies: Tapping the Power of Nature (EHT-TPN 2024), was planned well in advance and articulated as per the expectation of the funding bodies and sponsorers. This is the third conference in a span of six years, that was organized by the department with the support of various Government funding agencies. It was planned according to the aspirations of UN Sustainability Development Goals.

I believe that the conference has been a remarkable event, which brought a diverse group of experts, scientists, academicians and scholars together to explore and discuss the latest advancements in energy harvesting technologies. There were eight insightful lectures by seven speakers. There were ten plenary talks and sixteen poster presentations. Key note speaker,

Dr Shaikh Faruque Ali, Professor, Department of Applied Mechanics, IIT Madras spoke on Energy in small scale: Need to scale up. The talk was very insightful and discussed all futuristic possibilities of energy harvesting.

Dr Praveen C Ramamurthy, Professor, Department of Materials Engineering, Indian Institute of Science, Bengaluru, spoke on the topic of Molecules to devices: Organic Electronics, which explored the role of Chemistry in sustainable energy harvesting options.

Dr K S Narayan Professor, Chemistry and Physics of Materials Unit, JNCASR, Jakkur, Bengaluru discussed the role of technology in developing solar cells. The title of his talk was "Recent advances in solar cells".

Dr Nagesh S Kini, Co-Founder & Chief Technology Officer, Vimano EWA Pvt. Ltd. Bengaluru spoke on the topic "The future large scale energy storage". He narrated the importance of Flow batteries in the future which can meet the energy needs.

Dr Vasudha Hegde, Professor, Department of Electrical & Electronics Engineering,

Nitte Meenakshi Institute of Technology, Bengaluru, highlighted the application of Piezoelectric materials and devices.

Dr Anindita Roy, Associate Professor, Department of Mechanical Engineering, Symbiosis Institute of Technology, Maharashtra gave two lectures on Aerodynamics and wind energy conversion efficiency and Batteries used in off-grid Solar Power Plants and Procedures for Performance Improvement.

Dr P.M. Aneesh, Assistant Professor, Department of Physics, Central University of Kerala discussed the topic " Two dimensional materials: Current trends and future directions"

I am confident that EHT-TPN 2024 has fulfilled its purpose in meeting the expectations of young researchers and it has exposed them towards new opening of research in the field of energy harvesting.

I thank the sponsors of this National Conference: The Science and Engineering Research Board (SERB), the Department of Science and Technology (DST), and Mangalore Refinery and Petrochemicals Limited (MRPL).

I extend my sincere gratitude to all the authors who contributed articles to the “Proceedings of the National Conference on Energy Harvesting Technologies: Tapping the Power of Nature.”

I Congratulate the Organizing Secretary **Dr E. Deepak D'silva** who worked tirelessly for the success of the conference and edited this volume of conference proceeding. I also wish to express my sincere gratitude to all members of Organizing committee and Advisory committee for their valuable suggestions. Special thanks to My Colleagues in the department without whom the conference would not have realized.

I hope that many more such events can be organized by the department in the future.

Dr Chandra Shekhara Shetty T

Convener- EHT-TPN 2024

Table of Contents

Flexible Polyvinyl Alcohol-Expanded Graphite-based Triboelectric Nanogenerator: Efficient Energy Harvesting for Self-Powered Electronics

Sebghatullah Amini[1], Rumana Farheen Sagade Muktar Ahmed[1], Sangamesha Madanahalli Ankanathappa[2], Krishnaveni Sannathammegowda[1,*]

[1] *Department of Studies in Physics, University of Mysore, Mysuru 570006, Karnataka, India*
[2] *Department of Chemistry, The National Institute of Engineering, Mysuru 570008, Karnataka, India*

*Email: sk@physics.uni-mysore.ac.in

Abstract

In the present study, a flexible Polyvinyl Alcohol-Expanded Graphite-based triboelectric Nanogenerators (PEGr-TENG) is designed to harvest low-frequency mechanical vibrations and convert them into electricity. The device is fabricated using a Polyvinyl Alcohol-Expanded Graphite (PVA-EGr) composite film as the tribopositive layer, Polyurethane (PU) as the tribonegative layer, and aluminum (Al) foil tape as the electrode. The morphological and elemental analysis of the pristine PVA and composite layers was conducted using SEM and EDS. Electrical characterization of the fabricated devices revealed that the PEGr-TENG with 0.4 g of EGr generated the highest output which is utilized for further characterizations and applications. The device is demonstrated to charge several capacitors and power a series of LEDs, showcasing its practical application in self-powered electronics.

Keywords: Triboelectric nanogenerator, expanded graphite, self-powered devices, energy harvesting, wearable electronics

1 Introduction

In today's energy-demanding world, triboelectric nanogenerators (TENGs) have emerged as transformative devices capable of harnessing mechanical motion to generate electrical power. These devices, operating on the principles of triboelectrification and electrostatic induction, are essential for driving the evolution of self-sustaining technologies [1]. The selection of materials for TENG fabrication plays a pivotal role in optimizing performance, with each component contributing significantly to the device's efficiency and output [2].

Expanded graphite (EGr) stands out as a crucial material in TENG fabrication due to its excellent electrical conductivity and high surface area, enhancing the triboelectric effect and improving electrical output performance [3]. Polyvinyl Alcohol (PVA) is a water-soluble synthetic polymer known for its film-forming properties. It is utilized in TENGs for its flexibility, mechanical strength, and ability to form uniform films,

essential for effective triboelectric performance [4]. Integrating EGr into the PVA matrix creates a composite material that significantly enhances triboelectric performance and overall device efficiency.

In this study, a flexible Polyvinyl Alcohol-Expanded Graphite-based TENG (PEGr-TENG) is fabricated. To understand the impact of EGr on the electrical output performance of TENG, five different devices were fabricated with varying concentrations of EGr in the PVA matrix (0.1, 0.2, 0.3, 0.4, and 0.5g). The optimized device underwent further characterization and application testing to demonstrate its potential in practical, self-powered electronics.

2 Experimental details

EGr was obtained from Sd fine-chem. Ltd., India. Commercial Al foil tape was utilized to assemble the TENG devices. The materials and the preparation of PU film is discussed in our previous work [5]. To prepare a homogeneous PVA solution, 100 ml of deionized (DI) water is heated to 60 °C in a beaker, and 7 g of PVA powder is slowly added and stirred with a magnetic stirrer for 20 minutes. Then, 0.4 g of EGr

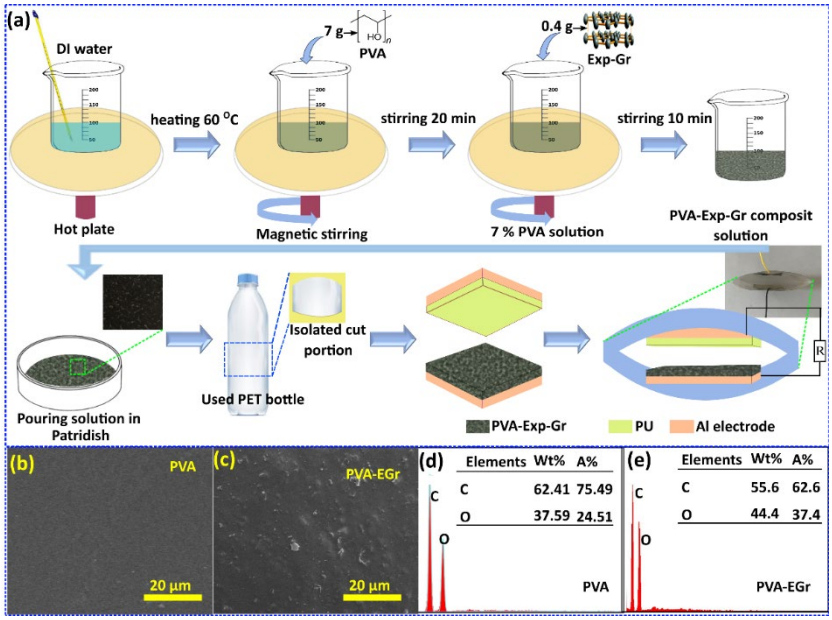

Fig. 1 (a) The schematic illustration of PVA-EGr solution formation and the device fabrication. SEM image of (b) pristine PVA and (c) PVA-EGr composite film. EDS spectrum of (d) pristine PVA and (e) PVA-EGr composite film.

powder is added to the PVA solution and stirred for an additional 10 minutes to achieve a uniform composite solution, maintaining the temperature at 60 °C. The solution is cast into a petri dish and allowed to dry at room temperature for 2 days and the dried film is carefully peeled off (Fig. 1a).
To fabricate the device, a section of a polyethylene terephthalate (PET) waste-water bottle was utilized, as detailed in our prior research [6]. The PU layer and PVA-EGr composite film were cut into 4 x 4 cm^2 dimensions, pasted on Al foil tape, and used as the top and bottom triboelectric layers. The frictional layers were adhered to the inner surface of the water bottle, forming an arch-shaped structure. The photographic image of the device is depicted in the inset Fig. 1a.

3 Results and discussion

Surface morphology and elemental composition of the prepared films were studied using scanning electron microscopy coupled with energy-dispersive X-ray spectroscopy (SEM with EDS, Zeiss EVOLS15, Germany). The SEM image of pristine PVA (Fig. 1b) reveals a flat and smooth surface, indicating the uniformity of the thin film. In contrast, the SEM image of the PVA-EGr composite film demonstrates a uniform distribution of EGr particles, which increases surface roughness and contact surface area, thereby enhancing the triboelectric performance of the device (Fig. 1b). The EDS spectrum of pristine PVA film (Fig. 1c) shows the expected C and O content, validating its purity. In contrast, the EDS spectrum of PVA-EGr composite film (Fig. 2d) exhibits higher C content, which improves surface charge density and performance of the PVA-EGr TENG [7].

The electrical measurements were conducted using a Keithley source measure unit (model 2460, USA). The electrical properties of PEGr-TENG devices were investigated in vertical contact-separation mode. The device was attached to a custom linear motor for consistent contact and separation, with a 4 x 4 cm^2 active area and a 2 cm gap between layers. When an external force brings the layers into contact, contact electrification takes place, transferring electrostatic charges to their surfaces, creating surface charge density. Upon releasing the force layers separate from each other, inducing a potential difference, which drives electron flow through an external load. Electron accumulation depends on the gap distance, diminishing to zero at maximum separation (2 cm). Reapplying the force causes charges to flow in the opposite direction due to electrostatic induction, initiating a negative current cycle. This continuous contact-separation cycle generates alternating current (AC) by TENG devices.
The generated voltage and current of PEGr-TENGs with varying EGr concentrations were analyzed. Increasing the filler concentration enhances the output performance up to a certain point (0.4g). Beyond this optimal concentration, further increases lead

to a reduction in output due to the agglomeration of nanoparticles in the composite film, as detailed in Table1. The output behavior of the optimized device was analyzed

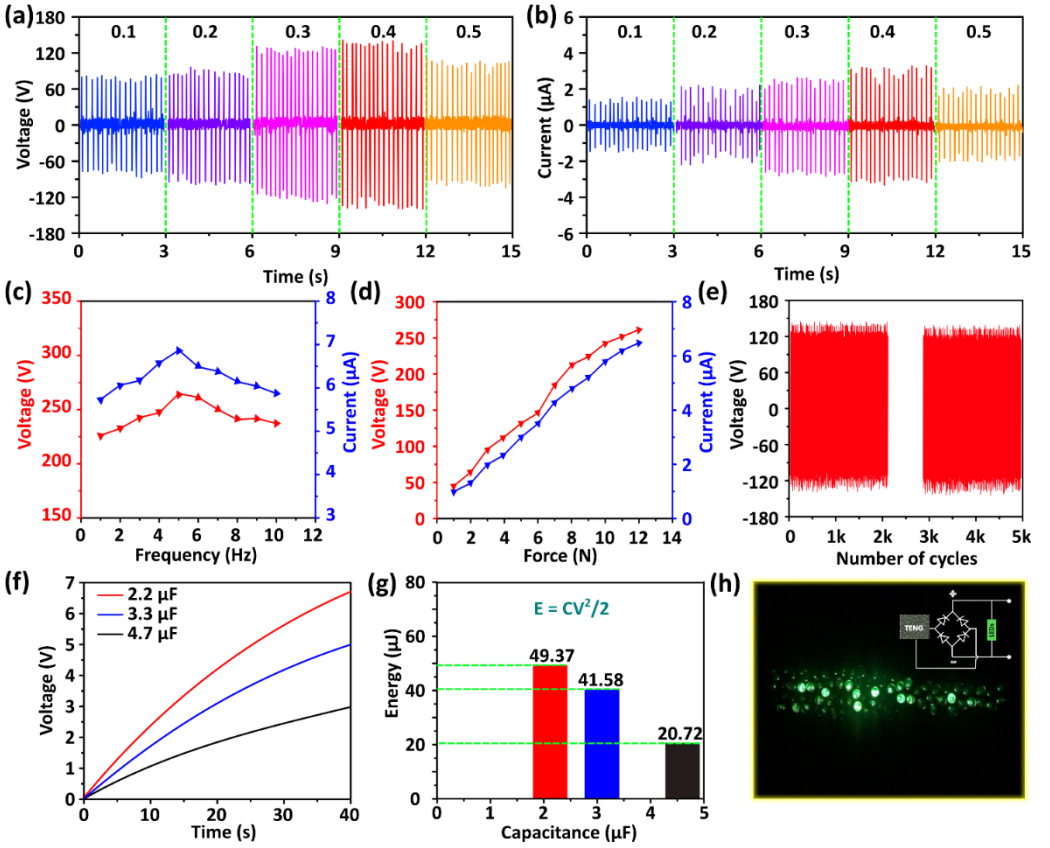

with varying operational frequencies. Both generated voltage and current increased

Fig. 2 (a) The generated voltage and (b) current signals by PEGr-TENG. (c) The output performance with respect to varying operational frequency. (d) The generated voltage and current behavior with increasing applied force. (e) The electrical stability test. (f) The charging curves of the capacitors. (g) The energy stored in each capacitor. (h) Powering LEDs (Inset Fig.; circuit diagram).

with the frequency up to 5 Hz, the device's resonance frequency. Beyond this threshold, the output reduced due to rapid contact separation, preventing the frictional layers from reaching their maximum separation distance (Fig. 2c). The output performance of the device was studied under varying applied forces, showing that both voltage and current increased with applied force (Fig. 2d). Mechanical durability and electrical stability were tested over 5000 cycles, with no visible fluctuations in output (Fig. 2e), demonstrating the device's robustness and reliability.

Frictional layers		Electrical output performance	
Bottom	**Top**	**Voltage (V)**	**Current (μA)**
PVA-EGr (0.1g)	PU	164.23	3.41
PVA-EGr (0.2g)		180.54	4.38
PVA-EGr (0.3g)		248.31	5.39
PVA-EGr (0.4g)		**264.68**	**6.87**
PVA-EGr (0.5g)		228.81	4.13

Table1: Electrical output performance of PEGr-TENG.

Further, the practical application of the PEGr-TENG was demonstrated by charging three commercial capacitors (2.2 μF, 3.3 μF, and 4.7 μF) to 6.7 V, 5.02 V, and 2.97 V, respectively (Fig. 2f). The energy stored, calculated using $E = ½ CV^2$, showed the 2.2 μF capacitor stored 49.37 μJ, which can be used to power small electronics (Fig. 2g). The device also powered 82 green LEDs (Fig. 2h), showcasing its potential for self-powered electronics.

4 Conclusion

In this study, we developed a PEGr-TENG device using PVA-EGr composite films and PU layer as frictional layers and Al electrodes. SEM and EDS analyses confirming enhanced surface roughness and carbon content, improving performance of TENG device. Electrical tests showed optimal output with EGr concentrations up to 0.4g and at 5 Hz frequency. The device demonstrated mechanical durability over 5000 cycles and successfully charged capacitors and powered LEDs, showcasing its potential for self-powered electronics. This work highlights the device's efficiency and robustness in energy harvesting applications.

Acknowledgement

All the authors are greatly indebted to their respective organizations. Sebghatullah Amini and Rumana Farheen S.M. acknowledge Government of India for the financial support.

References

1. R. F. S. M. Ahmed, S. Amini, S. M. Ankanathappa, K. Sannathammegowda, Electricity out of electronic trash: Triboelectric nanogenerators from discarded smartphone displays for biomechanical energy harvesting, *Waste Manag.* **178** 1–11 (2024)
2. A. Yu, Y. Zhu, W. Wang, J. Zhai, Progress in triboelectric materials: toward high performance and widespread applications, *Adv. Funct. Mater.* **29** 1900098 (2019)

3. M. Ghozali, E. Triwulandari, W. K. Restu, Biopolymers in electronics, *Biopolym. Recent Updat. Challenges Oppor.* 289–321 (2022)
4. S. Amini, R. F. Sagade Muktar Ahmed, S. Madanahalli Ankanathappa S and S. K., Polyvinyl alcohol-based Economical Triboelectric Nanogenerator for Self-powered Energy Harvesting Applications, *Nanotechnology* **35** 035403 (2023)
5. R. F. S. M. Ahmed, S. K. K. Swamy, G. S. Chandrasekhar, S. M. Ankanathappa, A. Chandrasekhar, K. Sannathammegowda, Clitoria Ternatea Flower Extract: Biopolymer Composite-Based Triboelectric Nanogenerator as a Self-Powered Smart Counter, *Surfaces and Interfaces* 103369 (2023)
6. S. Amini, R. F. S. M. Ahmed, S. M. Ankanathappa, S. J. Shetty, T. K. Nanditha, S. C. Gurumurthy, K. Sannathammegowda, 2024 Robust PVA-MWCNTs-based Triboelectric Energy Harvesting Device: Self-powered Smart-door Technology, *Surfaces and Interfaces* 104775 (2024)
7. H. Wang, M. Shi, K. Zhu, Z. Su, X. Cheng, Y. Song, X. Chen, Z. Liao, M. Zhang, H. Zhang, High performance triboelectric nanogenerators with aligned carbon nanotubes, *Nanoscale* **8** 18489–94 (2016)

Mathematical Modelling and Simulation of NACA 0012 Aerofoil Characteristics and Force Distribution

Tejas Raghv [1,*], Praveen Prakash D'Souza [2]

[1] *Ramaiah University of Applied Sciences, Bengaluru - 500058, INDIA*

[2] *Physics Department, St Aloysius College (Deemed to be University), Mangaluru - 575003, INDIA*

* E-mail: tejas.toolshed@gmail.com

Abstract

The work demonstrates the forces acting on the NACA 0012 symmetrical aerofoil, whose simulation is performed on ANSYS. Since the NACA 0012 is a symmetric aerofoil, the above and below characteristics appear to be the same for a 0 degree angle of attack. Therefore, the simulation generates a more pronounced effect by increasing the angle of attack, which generates a larger lift force on the aerofoil. The corresponding pressure plot indicates a region of higher pressure under the aerofoil and lower pressure above it, which gives rise to the thrust. In addition, the output identifies the 1-D Plots of lift and drag coefficients to converge to a reasonable value over a period of 1000 iterations. Thus, the work addresses the design, mathematical modeling, iteration, pressure coefficient contour and calculation of aerofoil characteristics, which depend on variables such as the Angle of Attack and Reynold's number.

Keywords: Aerodynamics; ANSYS; NACA 0012; Reynold's Number; Lift; Drag

1 Introduction

The pressure contour is useful in understanding the workings of an aerofoil. The pressure plot indicates a region of higher pressure under the aerofoil and lower pressure above it. This pressure difference gives rise to the thrust force. Since the NACA 0012 is a symmetric aerofoil, for a zero degree angle of attack the top and bottom regions appear to be the same. A more pronounced effect can be obtained by increasing the angle of attack, which generates a larger lift force on the aerofoil. However, the angle of attack can only be increased until a certain extent or the plane will begin to stall, where the change in the angle of attack has no effect on the lift. Stall condition gives rise to instability by causing recirculation along the foil.[1] In this paper, we attempt to simulate the NACA 0012 aerofoil characteristics using ANSYS for computational fluid modeling.

2 Materials and Methods/Model

Data points of the NACA0012 aerofoil are obtained from the UIUC database. These data points must be edited in Excel as per Ansys convention to include grid numbering and axis formatting. The simulation is performed as a workbench project using *DesignModeler*. The .txt dataset that corresponds to the NACA 0012 geometry is plotted as a 3d curve. *Lines from Points* option is used to connect the edges to make an aerofoil surface. The chord length is set to 1m, while the radius of the circle must be 10m (10c) and the length of the rectangle is taken as 20m (20c). The *Surface from Sketch* option is used to convert the sketch to a surface by selecting the bounding sketch layout. To set up the geometry for Meshing, the outer domain is split along the ZX axis before generating Face splits until it gives rise to a total of 6 parts within the domain. For a CFD simulation to work, we need to treat the surface as a fluid. Hence, use the *2 Parts, 2 Bodies* option and select the *Surface body* to define Fluid/Solid dropdown as *Fluid.*

The build can be meshed, where the *Face Mesh* uses the *Quadrilateral Method*. The top left and bottom boundaries of the outer domain is set and named as the *Inlet.* However, the right-most boundary wall is set as an *Outlet.* The aerofoil boundaries (including the small trailing edge) is set as the *Aerofoil Wall. T*he *Element Type* is swapped with *Number of Divisions* and defined to be 100. The mesh is performed with an intent to design a high concentration of the mesh along the surface of the aerofoil. It is essential to change the capture curvature to *No* to find the *Edge sizing* behavior, which is set as *Hard.* A *Bias* of Increasing line length is added with a *Bias factor* to 500. This would have generated a bias of favoring more mesh density towards the aerofoil. The *Sizing* and *Bias* are adjusted until there is a large Mesh concentration near the Aerofoil. The Mesh is observed for inconsistencies - if certain geometric segments are deformed - the *Capture curvature* option could offer a better rendition.

The simulation inputs are fed into the solver to study the performance of the aerofoil at different conditions. This simulation runs on the default *Pressure Based* and *Steady State Solver,* where the *Viscous (SST k-Omega)* is selected for the *Model*. It is excellent in predicting aerofoil separation and recommended for most aerofoil simulations. [3] To simulate a wind tunnel air flow the *Inlet Boundary conditions* are set to 30 m/s along the *X axis* as a back test parameter. The *Outlet Pressure Boundary Condition* adds a constant pressure to the ends of the domain. The *Solutions* obeys the *Coupled* numerical scheme, using the *Second Order Upwind* for higher accuracy. Lift and Drag are added to *Report Definition,* while ensuring the variables used are marked with the right axes. Eg. Lift uses Y=1, while Drag uses X=1. Under *Monitors* the *Residuals* help set an acceptable convergence value such as 1e-6. Using a hybrid *Initialization,* the calculation is *Run* at 1000 iterations.

3 Results and Discussions

Air is assumed as the outer fluid, with default density of 1.225 kg/m^3 and default viscosity of 1.7894x10^{-5} kg/(ms). We perform a Wind tunnel simulation for a Chord Length of 1m and a Reynold's number of 3x10^6 at a 4-degree Angle of Attack. From $Re = \frac{\rho v L}{\mu}$ we obtain $v = \frac{3 \times 10^6 \times 1.7894 \times 10^{-5}}{1.225 * 1}$ = 43.82204082 m/s. The X and Y vector for the velocity inlet was found to be $43.82204082 \times cos(4) = 43.71529253\, m/s$ and $43.82204082 \times sin(4) = 3.05687104\, m/s$. The Drag Inputs are cos(4) = 0.9975640503 and sin(4) = 0.0697564737, while the Lift inputs are - sin(4) = -0.06975647374 and cos(4) =0.9975640503 for the X and Y vectors.

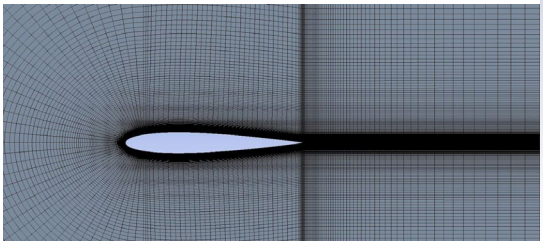

Fig. 1 Geometry and Meshing

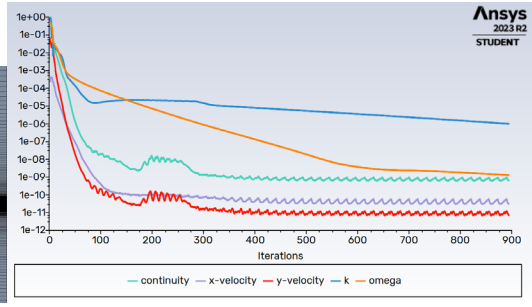

Fig. 2 Scaled Residuals

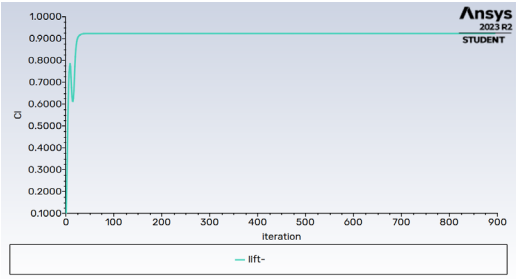

Fig. 3 Converged Lift Plot

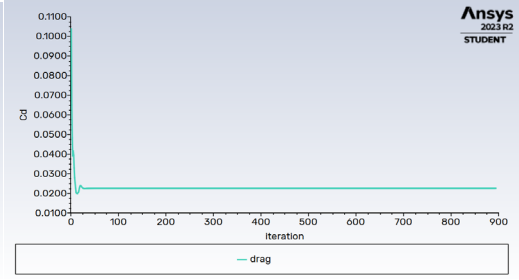

Fig. 4 Converged Drag Plot

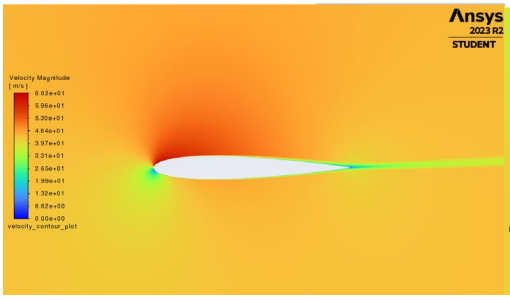

Fig. 5 Velocity Contour Plot

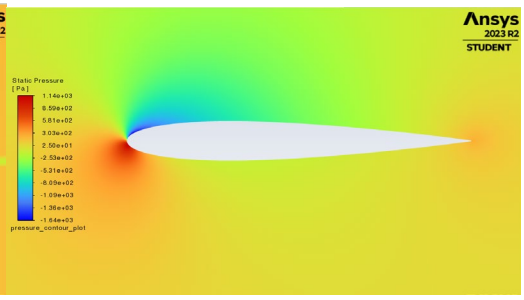

Fig. 6 Static Pressure Contour Plot

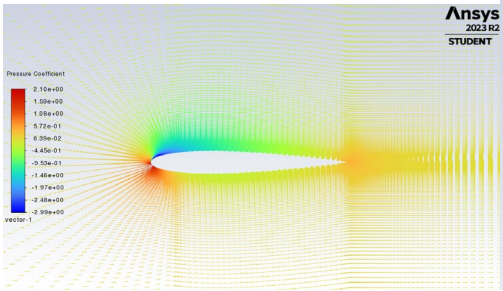

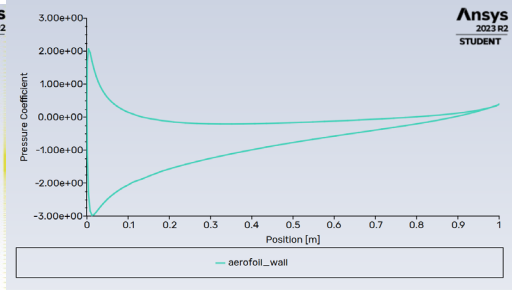

Fig. 7 Pressure Coefficient Vector Plot **Fig. 8** Pressure Coefficient Distribution

The above outputs are rendered for a 4-degree angle of attack. As Lift acts at a perpendicular, we obtain the above values through trigonometry. Above, the Lift and Drag components are depicted using X and Y components to interpret force vectors parallel to the flow. Furthermore, the density and viscosity of air changes with temperature and altitude.[2] Hence, for a simulation of an aerofoil at 10,000 ft would require modifications for the preliminary constants.

4 Conclusions

The 1d Plots of lift and drag coefficient converge to a reasonable value over a period of 1000 iterations. The flow field was illustrated by the use of velocity magnitude vectors or pathlines to depict the streamlines passing through the aerofoil. The velocity contour plot illustrates a stagnation point on the leading edge with a discontinuity at the trailing edge, which creates a streak in the streamline all the until the domain edge. The velocity at the stagnation point is zero and increases past the point. The flow also depicts a loss in moment and slows down as it passes along the trailing edge. Furthermore, due to the no slip condition, the velocity is observed to be almost zero at the wall and slowly increases as it is away. Therefore, the simulation was able to successfully demonstrate the NACA 0012 characteristics of streamline flow, velocity and pressure distribution. The outputs and the results are in accordance with the initial investigation outline.

References

1. J. D. Anderson, G. Degrez, E. Dick, R. Grundmann, *Computational fluid dynamics: an introduction*, 2013.
2. T. Anthony (2021). ANSYS Fluent NACA 4412 (or NACA 0012) 2D airfoil CFD Tutorial with Experimental Validation [online]. https:// www.youtube.com/watch?v=nzvEvLCxOss&t=5s
3. Tamas Aero (2018). NACA 0012 CFD analysis Ansys Fluent Part 1: Generate Geometry [online].

Design, fabrication, and application study of polyvinyl chloride multiwall carbon nanotubes based triboelectric nanogenerators

L Adarsh Raj[1], Sebghatullah Amini[1], Rumana Farheen Sagade Muktar Ahmed[1], Sangamesha Madanahalli Ankanathappa[2], Gurumurthy S C[3], Krishnaveni Sannathammegowda[1,*]

[1] Department of Studies in Physics, University of Mysore, Mysuru 570006, Karnataka, India
[2] Department of Chemistry, The National Institute of Engineering, Mysuru 570008, Karnataka, India
[3]Nano and Functional Materials Lab (NFML), Manipal Institute of Technology, Manipal Academy of Higher Education, Manipal- 576104, Karnataka, India.

*Email: sk@physics.uni-mysore.ac.in

Abstract

Triboelectric nanogenerators (TENGs) have emerged as cutting-edge technology in the fields of nanoenergy and nanotechnology. In the present study, a flexible polyvinyl chloride multiwall carbon nanotube-based TENG (PMC-TENG) with dimensions of 4 x 4 cm² was designed to harvest low-frequency mechanical vibrations and convert them into electricity. The device was fabricated using a composite film of polyvinyl chloride (PVC) and multi-walled carbon nanotubes (MWCNTs) with varying concentrations of MWCNTs as the tribonegative layer, and aluminum (Al) as both the tribopositive layer and electrode. Morphological and elemental analyses of the composite layers were conducted using scanning electron microscopy (SEM) and energy-dispersive X-ray spectroscopy (EDS). Electrical characterization of the devices revealed that the PMC-TENG containing 0.028 g of MWCNTs generated the highest output, achieving a voltage of 150.43 V and a current of 2.418 μA. Furthermore, the electrical output generated by the TENG was employed to charge capacitors and power light-emitting diodes (LEDs). These findings suggest that incorporating MWCNTs into the PVC matrix enhances energy harvesting capabilities, thereby opening new avenues for self-powered applications.

Keywords: Triboelectric nanogenerator, multiwall carbon nanotubes, energy harvesting, self-powered devices.

1 Introduction

Triboelectric nanogenerator (TENG) harnesses various low-frequency mechanical energies present in the ambient environment into electrical energy, making it a versatile and sustainable solution for powering portable electronics and self-powered sensing applications [1]. The underlying mechanism of TENGs involves two key phenomena: triboelectrification, which is the generation of electrical charge through the frictional contact between different materials, and electrostatic induction, which is

the generation of electric potential due to the separation of charged surfaces. When two materials come into contact and then separate, electrons transfer from one material to the other, creating a charge imbalance. This charge imbalance induces an electric potential difference, which can be harnessed as electrical energy. Compared to other energy harvesting technologies, TENGs are distinguished by their high instantaneous output power, a broad selection of available materials, eco-friendly and cost-effective fabrication processes, and the ability to be customized for various working modes tailored to specific applications [2].

Polymers are widely used materials for TENG fabrication because of their lightweight features, easy processability, durability, and tannable surface properties [3]. In the present work, PVC has been utilized along with different concentrations of MWCNTs to fabricate the TENG devices. The electrical performance of the devices was checked and the optimized device with additional characterization is demonstrated for applications to showcase its viability for use in wearable electronics and self-powered sensors [4].

2 Experimental details

Polyvinyl chloride (PVC) was obtained from Sd Fine-Chem Ltd., India, and multi-walled carbon nanotubes (MWCNTs) were procured from Adnano Technologies Pvt. Ltd., India Commercial aluminum (Al) foil tape was used to assemble the TENG devices. To prepare the PVC-MWCNT composite thin film, 10 g of PVC powder was dissolved in 100 ml of tetrahydrofuran (THF) solvent and stirred using a magnetic stirrer for 10 minutes to create a 10% PVC solution. Subsequently, incremental amounts of MWCNTs (0.007, 0.014, 0.028, 0.056, and 0.112 g) were added to the PVC solution with an additional stirring period of 10 minutes to ensure uniform dispersion. The resulting PVC-MWCNT solution was cast into a petri dish and allowed to air-dry at room temperature for 24 hours, forming a thin film. This thin film was then carefully peeled off from the petri dish for further applications (Fig. 1a) [5].

The PMC-TENGs were fabricated using the common PVC-MWCNT composite film as one frictional layer and an aluminum sheet as the opposite frictional layer. The aluminum sheet served as both the top and bottom electrodes of the TENG devices. The frictional layers were cut into 4 x 4 cm^2 dimensions and adhered to the Al foil tape. The fabricated device was placed inside an arc-structured cut portion of a polyethylene terephthalate (PET) waste-water bottle to enhance its stability (Fig. 1b).

3 Results and discussion

The surface morphology and elemental composition of the prepared films were analyzed using scanning electron microscope (SEM) coupled with energy-dispersive

X-ray spectroscopy (EDS), utilizing a Zeiss EVO LS15 (Germany) [6]. The SEM image of the PVC-MWCNT film (Fig. 1d) shows a uniform distribution of MWCNT particles, which enhances surface roughness and contact surface area, thereby improving the triboelectric performance of the device (Fig. 1b) [7]. The EDS spectrum of the PVC-MWCNT film (Fig. 1e) confirms the presence of carbon (C) and oxygen (O), validating the material's purity. Additionally, the higher carbon content in the EDS spectrum increases surface charge density, further enhancing the performance of the PMC-TENG [8].

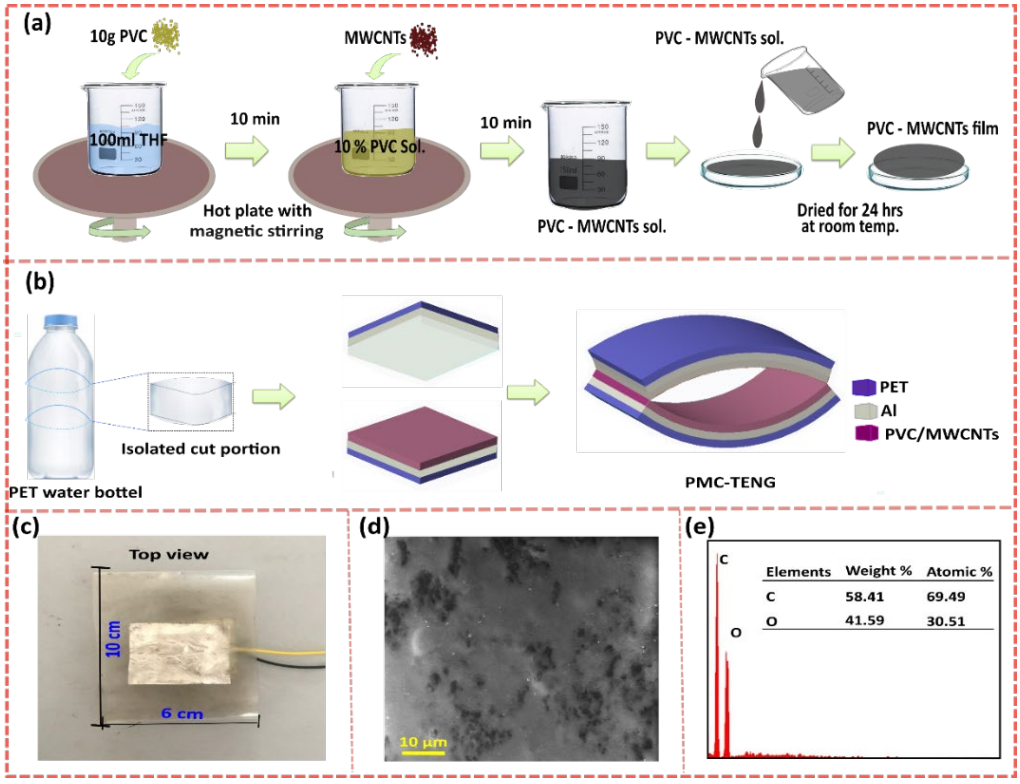

Fig. 1(a) The schematic illustration of PVC-MWCNTs film preparation and (b) Device fabrication. (c) Real image of fabricated PMC-TENG device. (d) SEM image and (e) EDS spectrum of PVC-MWCNTs composite film.

Electrical measurements were conducted using a Keithley source measure unit (model 2460, USA). The electrical properties of the PMC-TENG devices were investigated in a vertical contact-separation mode. The device, with an active area of 4 x 4 cm^2 and a 2 cm gap between the layers, was mounted on a custom linear motor to ensure consistent contact and separation. When an external force brings the layers into contact, contact electrification occurs, transferring electrostatic charges to their

surfaces and generating surface charge density. Upon release of the force and separation of the layers, a potential difference is induced, driving electron flow through an external load. The amount of electron accumulation depends on the gap distance, decreasing to zero at the maximum separation of 2 cm. Reapplying the force causes charges to flow in the opposite direction due to electrostatic induction, initiating a negative current cycle. This continuous contact-separation process generates alternating current (AC) in the TENG devices. The working mechanism of the device is illustrated in Fig. 2a.

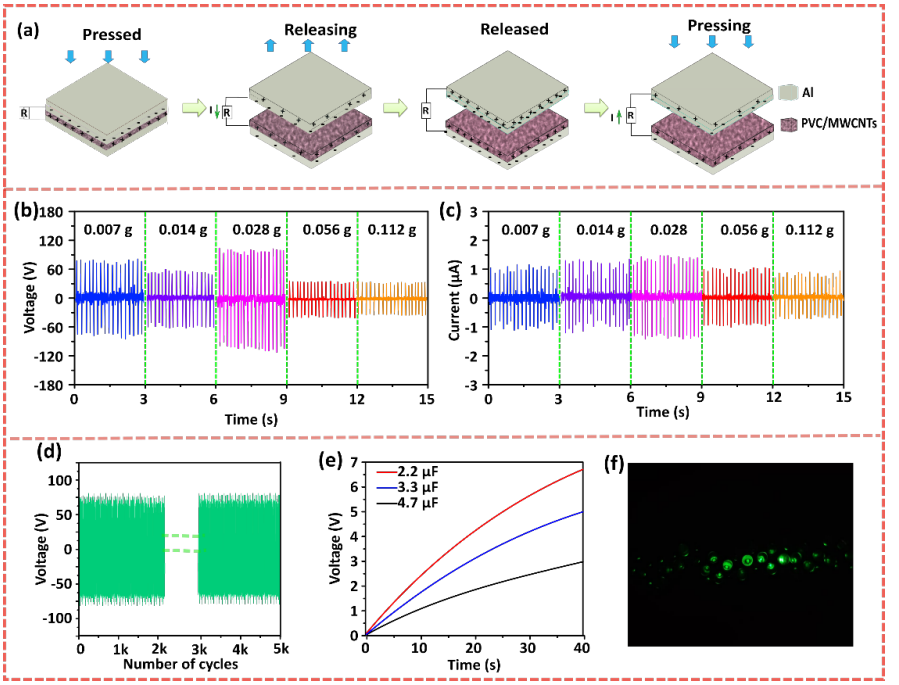

Fig. 2 (a) Working mechanism of the PMC-TENG **(b)** The generated voltage and **(c)** current signals by PMC-TENG. **(d)** The electrical stability test. **(e)** The charging curves of the capacitors. **(f)** Powering LEDs.

Table 1: Electrical output performance of PMC-TENG.

Frictional layers		**Electrical output performance**	
Bottom	**Top**	**Voltage (V)**	**Current (μA)**
PVC-MWCNTs(0.007g)	Al	133.23	2.13
PVC-MWCNTs(0.014g)	Al	112.87	2.40
PVC-MWCNTs(0.028g)	**Al**	**150.43**	**2.42**
PVC-MWCNTs(0.056g)	Al	80.38	2.00
PVC-MWCNTs(0.112g)	Al	76.11	1.89

The voltage and current generated by PMC-TENGs with different MWCNT concentrations were examined at an operating frequency of 6 Hz using a custom-made linear motor. It was observed that increasing the filler concentration enhanced the output performance up to an optimal point (0.028 g). Beyond this concentration, further increases led to a decline in output due to the agglomeration of nanoparticles within the composite film, as detailed in Table 1. The generated signals of voltage and current for different MWCNT concentrations are shown in Figs. 2b and 2c, respectively. Mechanical durability and electrical stability were tested over 5000 cycles, with no noticeable fluctuations in output (Fig. 2d), demonstrating the device's robustness and reliability. Additionally, the practical application of the PMC-TENG was demonstrated by charging three commercial capacitors (2.2 μF, 3.3 μF, and 4.7 μF) to 6.7 V, 5.02 V, and 2.97 V, respectively (Fig. 2e). The device also successfully powered 25 green LEDs (Fig. 2f), showcasing its potential for self-powered electronics.

4 Conclusion

In the present study, a PMC-TENG device has been developed utilizing PVC-MWCNTs composite films and an Al layer as frictional layers, paired with Al electrodes. SEM and EDS analyses confirmed increased surface roughness and carbon content, which enhanced the TENG device's performance. Electrical tests revealed optimal output with MWCNTs concentrations of 0.028g at an operating frequency of 6Hz. The device showed mechanical durability over 5000 cycles and successfully charged capacitors and powered LEDs, demonstrating its potential for self-powered electronics. This work underscores the device’s efficiency and robustness in energy-harvesting applications.

References

1. B. Ramasubramanian, S. Sundarrajan, R. P. Rao, M. V. Reddy, V. Chellappan, S. Ramakrishna, Novel low-carbon energy solutions for powering emerging wearables, smart textiles, and medical devices, *Energy & Environmental Science* **15**(12) 4928-4981 (2022)
2. W. G. Kim, D. W. Kim, I. W. Tcho, J. K. Kim, M. S. Kim, Y. K. Choi, Triboelectric nanogenerator: Structure, mechanism, and applications, *ACS nano* **15**(1) 258-287 (2021)
3. M. Shanbedi, H. Ardebili, A. Karim, Polymer-based triboelectric nanogenerators: Materials, characterization, and applications, *Progress in Polymer Science* 101723 (2023)
4. W. Tang, Q. Sun, Z. L. Wang, Self-powered sensing in wearable electronics—a paradigm shift technology, *Chemical Reviews* **123**(21) 12105-12134 (2023)
5. T. Arunkumar, R. Karthikeyan, R. Ram Subramani, K. Viswanathan, M.

Anish, Synthesis and characterisation of multi-walled carbon nanotubes (MWCNTs), *International Journal of Ambient Energy* **41**(4) 452-456 (2020)
6. J. Wen, H. He, C. Niu, M. Rong, Y. Huang, Y. Wu, (2022). An improved equivalent capacitance model of the triboelectric nanogenerator incorporating its surface roughness, *Nano Energy* **96** 107070 (2022)
7. M. Patel, S. Manna, A. Vo, X. Xu, D. Conti, S. Choi, J. Zheng, Scanning Electron Microscope (SEM) Coupled with Energy Dispersive X-ray Spectroscopy (EDS)-A potential analytical tool for physico-chemical characterization of API in complex drug formulations, *Microscopy and Microanalysis*, **26**(S2) 2254-2255 (2020)
8. C. Zhang, L. Zhou, P. Cheng, X. Yin, D. Liu, X. Li, J. Wang, Surface charge density of triboelectric nanogenerators: Theoretical boundary and optimization methodology, *Applied Materials Today* **18** 100496 (2020)

Synthesis and characterization of Optical and Dielectric properties of percentages of Ni-doped Zn_2TiO_4 nanopowders

Theope Raja G *, Balaji J
Department of Physics, University College of Engineering, Panruti- 607106.
*E-mail: theoperaj@gmail.com

Abstract

The 1%, 2%, and 3% percentages of Ni-doped Zn_2TiO_4 nanopowders were prepared by sol-gel technique and calcined at 800°C for 4 hours. The synthesized nanopowders exhibit cubic structure in all percentages of Ni-doped Zn_2TiO_4. FTIR and Raman spectroscopy ascertain the presence of ZnO and TiO_2. The thermal study is analyzed between 100°C to 400°C by thermogravimetric analysis. In diffused reflectance spectroscopy, doping of Ni as a percentage increases as the direct optical bandgap energy decreases to a lower energy band spectrum. The dielectric constant (k) and dielectric Loss (tan δ) decrease with increasing frequency in different temperature ranges in all doping percentages. The electrical conductivity (σ_{ac}) in all the percentages of Ni-doped Zinc titanate as increases with an increase in all temperatures which shows that nickel-doped zinc titanate nanopowders are suitable for optical behavior applications.

Keywords: Ni-doped Zn_2TiO_4, sol-gel method, optical band gap (E_g), dielectric constant & loss, AC conductivity.

1 Introduction

The transition metal oxide of NiO is a semiconductor nanoparticle with a wide optical band gap and remarkable dielectric properties. The physiochemical stability of NiO nanoparticles may be used in various technical applications. Due to the unique chemical stability of nickel on zinc sites, Ni-ZnO-TiO_2-based composites are considered the most efficient due to their improved optical, dielectric, and electrical properties. Few studies have been focused on understanding how Nickel doped with transition metal compounds affects its dielectric and conduction properties during low and high-temperature evolution [1-3]. This research article aims to investigate the synthesis and characterization of the structural, thermal, optical, and dielectric properties of various percentages of Ni-doped Zn_2TiO_4 NPs.

2 Material and method

Zinc acetate dihydrate, Nickel (II) nitrate hexahydrate, Titanium (IV) oxide, and Oxalic acid dehydrate are procured from Merck and utilized as purchased. Ethanol is used as the solvent. The sol-gel method of synthesizing a stoichiometry equimolar ratio of Zn_2TiO_4 precursor solution was formulated using a sol and gel procedure. All

percentages of Ni are added and form a homogenous mixture with Zn_2TiO_4. A cloudy greenish sol-gel suspension was obtained. The sol-gel is dried overnight and calcinated at 800°C for 4 hrs. Finally, the desired Ni-doped nanopowders are obtained.

3 Results and Discussion

The powder XRD results of Ni-doped Zn_2TiO_4 in all the NPs are in cubic phase with lattice constant a = b = c = 8.4190 Å. The structures of Zn $(Ni_{0.8}\ Zn_{0.2}\ Ti)\ O_4$ compound are identified with the help of JCPDS card No (01-080-1689) [3,4]. In the powder xrd pattern, the maximum peak intensities are obtained at 35.33° in the percentage of Ni-doped NPs and ascertain the structure formation. The powder XRD spectra of Ni-doped Zn_2TiO_4 in all the NPs are given in fig. (1)

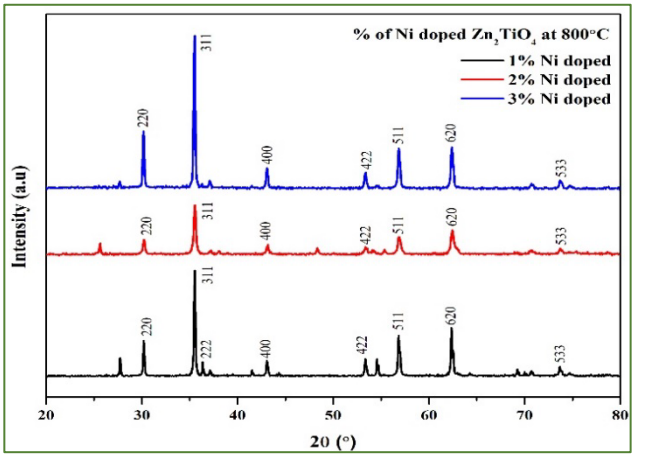

Fig. 1 Powder xrd of %s of Ni-doped Zn_2TiO_4 NPs.

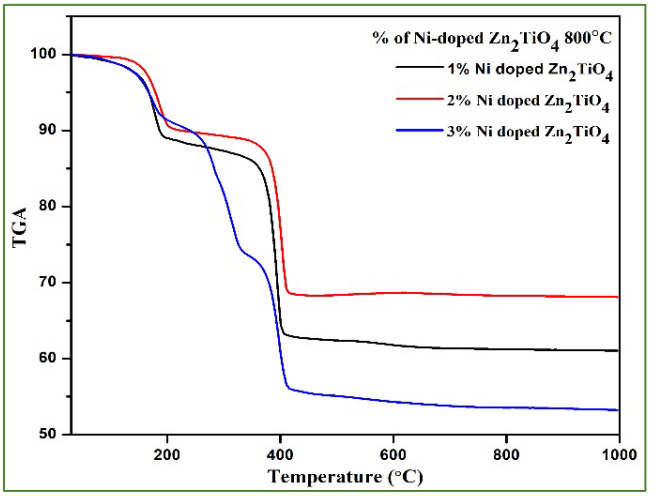

Fig. 2 TGA curve of %s of Ni-doped Zn_2TiO_4 NPs.

Figure 2. represents the TGA curve of Ni-doped Zn_2TiO_4. The weight loss percentage of all Ni-doped Zn_2TiO_4 NPs was found by TGA analysis between 100°C and 1000°C. The weight loss occurs in all Ni-doped Zn_2TiO_4 NPs starts at 175°C and exhibits two-stage decomposition.

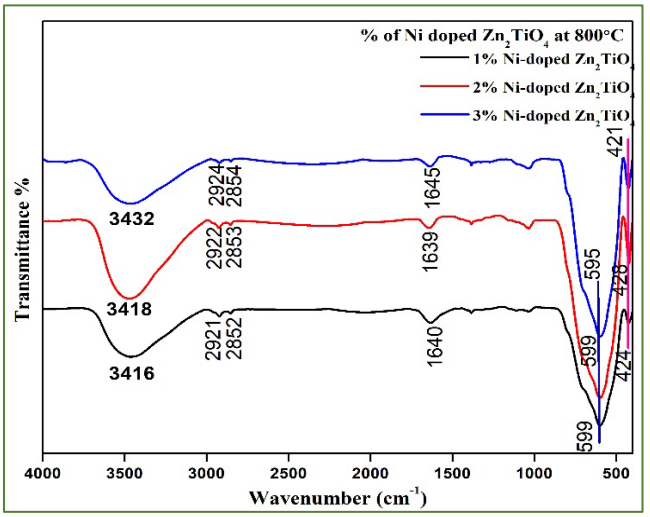

Fig. 3 (a) FTIR spectrum of %s of Ni-doped Zn2TiO_4 NPs.

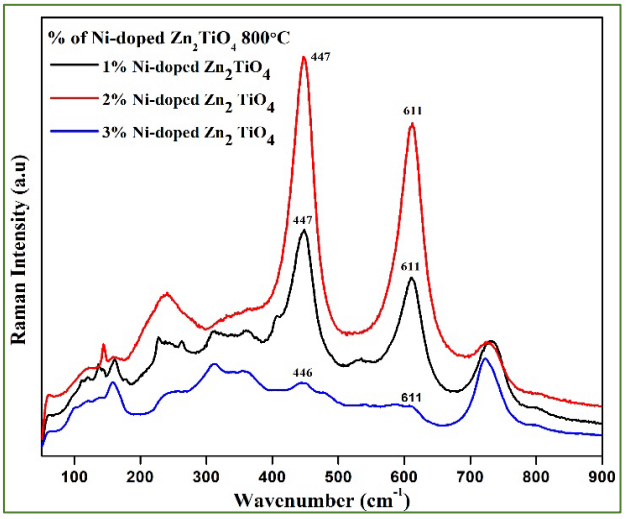

Fig. 3 (b) Raman spectrum of %s of Ni-doped Zn_2TiO_4 NPs.

Fig.3 (a & b) represents the FTIR and Raman spectra of all Ni-doped Zn_2TiO_4 NPs respectively. The vibrational band appeared at 599 cm^{-1} in FTIR and 611cm^{-1} in Raman representing the presence of Ti-O for all the percentages of Ni. Vibrational peaks appear at 421 to 424 cm^{-1} in FTIR and 447 cm^{-1} in Raman describing the

existence of Zn-O. The spectral intensity decreases and the peak becomes broader when the percentage of Ni in Zn_2TiO_4 increases [5, 6]. Wave number and Vibrational assignment of FTIR and Raman spectra of Ni-doped Zn_2TiO_4 NPs are shown in Table1.

Table 1: Comparison of FTIR and Raman spectra of %s of Ni-doped Zn_2TiO_4 NPs.

S. No	% of Ni-doped Zn_2TiO_4	FTIR (cm^{-1})		Raman (cm^{-1})	
		Zn-O	Ti-O	Zn-O	Ti-O
1.	1%	424	599	447	611
2.	2%	428	599	447	611
3.	3%	421	595	446	611

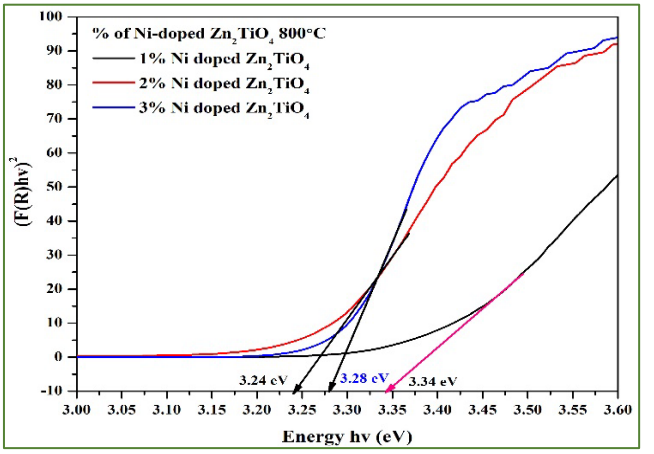

Fig. 4 Optical Bandgap (E_g) of %s of Ni-doped Zn_2TiO_4 NPs.

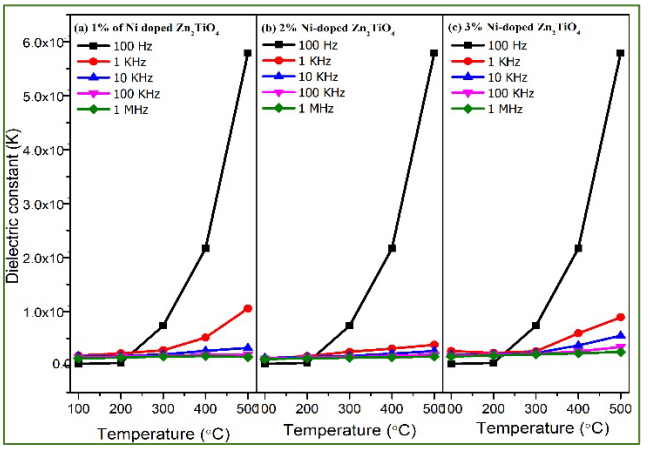

Fig. 5 (a-c) Dielectric constant of %s of Ni-doped Zn_2TiO_4 NPs.

Optical spectra of all Ni-doped Zn_2TiO_4 NPs are shown in Fig.4. In all Ni-doped Zn_2TiO_4 NPs the bandgap value of the materials is obtained between 3.24 eV to 3.34 eV and reveals that the band gap value decreases with increasing percentage of Ni.

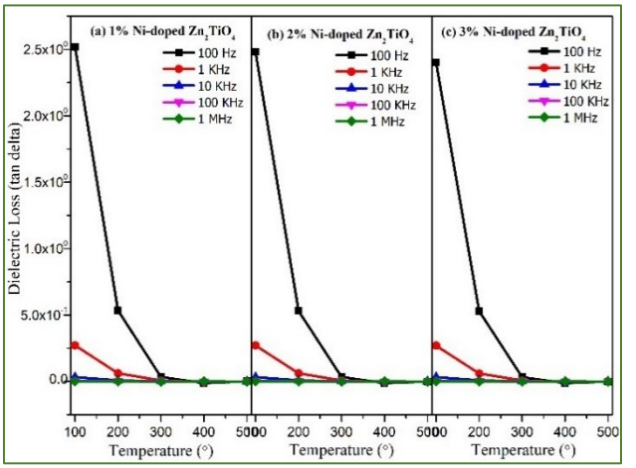

Fig. 5 (a-c) Dielectric loss of %s of Ni-doped Zn_2TiO_4 NPs.

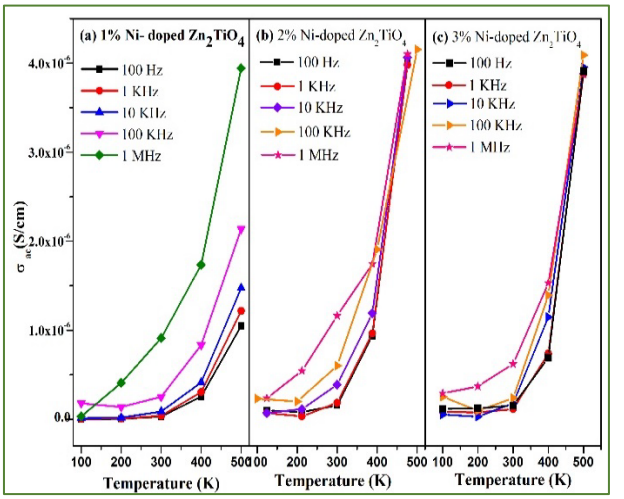

Fig. 6 (a-c) AC conductivity of %s of Ni-doped Zn_2TIO_4 NPs

The electrical property of NPs is obtained by analyzing the dielectric behavior of the synthesized nanoparticles concerning temperature and frequency [6-8]. The dielectric constant, dielectric loss, and ac conductivity of Zn_2TiO_4 NPs with different percentages Ni-doped are studied between 100Hz to 1MHz. The dielectric constant in all Zn_2TiO_4 NPs with different percentages Ni-doped having higher value at low frequency and decreases with increasing frequencies which represents that all types

of polarization are active at low frequency and inactiveness of space charge polarization in higher frequencies. The dielectric loss of all Zn_2TiO_4 NPs represents the good crystalline nature of the materials. Increasing ac conductivity with frequency is due to the polaron effect and ascertains the suitability of materials for optoelectronic applications.

5 Conclusion

Sol-gel synthesizing NPs with various percentages of Ni-doped Zn_2TiO_4 calcined at 800°C for 4 hours. The increase in doping percentage in the optical study is due to the decrease in energy bandgap. The higher dielectric constant (k) value at a low frequency of 100 Hz. The constant decreases with increasing frequency and acts as inactiveness of space charge polarization in higher frequencies of all the NPs. The loss factor (tan δ) decreases when temperature and frequency increase of very low-dielectric in all the percentages of Ni-doped Zn_2TiO_4 NPs. The ac conductivity increases with an increase in temperature and frequency in all the NPs. In all Percentages of Ni-doped Zn_2TiO_4 NPs increased ac conductivity due to the polaron effect and established the suitability of materials for optoelectronic applications.

Acknowledgments

We thank Alagappa University, IIT-Madras, and Pondicherry University for providing facilities for characterizations.

Reference

1. S. Karmakar, B. Panda, B. Sahoo, K. L. Routray, S. Varma, D.A Behera, *Materials Science in Semiconductor Processing* **88** 198-206 (2018)
2. R. Tursun, Y. C. Su, Q. S. Yu, J. Tan, T. Hu, Z. B. Luo, J. Zhang, *Journal of Alloys and Compounds* **773** 288-298 (2019)
3. A. F. Qasrawi, E. I. Sahin, M. Emek, *Journal of Electronic Materials* **50** 2223-2231(2021)
4. A. Bashir, A. Inayat, R. Bashir, S. Jamil, S. M. Abbas, M. Sultan, et al., *New Journal of Chemistry* **47**(7) 3560-3571 (2023)
5. T. Esaka, T. Ikebe, and M. Kamata, *Solid State Ionics* **76**(3-4) 237-242 (1995)
6. A. B. Abou Hammad, A. M. Mansour, A. M. El Nahrawy, *Physica Scripta* **96**(12), 125821 (2021)
7. D. Parajuli, P. Taddesse, N. Murali, K. Samatha, *Journal of the Indian Chemical Society* **99**(3), 100380 (2022)
8. S. Sapkal, P. Maske, H. S. Panda, *Bulletin of Materials Science* **47**(3), 125 (2024)

Developing *Borassus Flabellifer* Fruit husk Reinforced Polyester resin composite through open hand layup method

Jostol Len Pinto, Anikaramya. U, Kavya G K, Chethan G and Narayana Y*
Department of Physics, Mangalore University, Mangalagangotri – 574199

* E-mail: narayanay@mangaloreuniversity.ac.in

Abstract

In recent days, the preference for natural fibers over synthetic fibers as reinforcements in composite materials has increased due to their eco-friendliness, renewability, and sustainability. Composite materials known as "bio-composites" have either the reinforcement, the matrix, or both derived from biodegradable and renewable resources. This study investigates the development of natural fiber composites using polyester resin as a matrix and Borassus flabellifer fruit fibers (BFF) as the reinforcement, sourced from South Coastal Karnataka, to assess their effectiveness as sustainable composite reinforcements. The BFF fibers are extracted through the retting method to ensure purity. The composites are fabricated using the open hand layup method in a 300mm x 200mm open mold. Variations in fiber and matrix ratios from 1:30, 1:40, 1:50, 1:60 and 1:70 are used in the fabrication process. The open hand layup method involves lubricating or waxing the mold surface, applying a primary layer of matrix to the mold before placing the fiber into the mold, then placing a layer of BFF fiber over the pre-applied resin mold. The fiber is evenly spread using a brush, and a secondary finishing layer of matrix is poured into the mold to ensure even packing and distribution of matrix material throughout the mold. After 60 minutes, the developed composite is removed from the mold and placed under heavy weight for curing for about 24 hours. The findings of this study provide valuable insights into optimizing the utilization of BFF in eco-conscious engineering applications, promoting sustainable practices in material science and composite technology.

Keywords: Natural fiber, Natural fiber composite, Resin Composite, Thermosetting Composite.

1 Introduction

Biocomposites, also known as composite materials, have reinforcements, matrices, or both that are sourced from biodegradable and renewable resources. Typically, the matrix is either synthetic or a biopolymer, while the reinforcement is usually biological. The growing interest in biocomposites can be largely attributed to their cost-effectiveness and environmental benefits. These materials are generally less

expensive and have a reduced carbon footprint compared to traditional composites. Additionally, biocomposites offer reduced weight, enhanced functionality (such as impact absorption and damping), and improved occupational health safety [1].
In the European Union, over 95% of biocomposites produced for industrial applications are utilized in non-structural automotive components. These applications include waterproofing tiles, tabletops, interior design elements, containers, pots, headrests, front and rear panels, armrests, and trunk liners. Given that plastic does not decompose, there is an urgent need to reduce plastic usage across communities. Synthetic fibers pose threats to both the environment and human health. Natural fibers, derived from various parts of plants like fruits, stalks, roots, and leaves, consist of cellulose, hemicellulose, and lignin. Factors such as hydrophobic nature, strength, orientation, extraction processes, and treatment methods influence the performance of natural fibers. The strongest and stiffest organic material in the fibers is cellulose. The composition is 60–80% cellulose, 10–20% hemicelluloses, 5–20% lignin, and up to 20% moisture are often found in the fibers [2].

2 Materials and Methods

Borassus Flabellifer fruit is collected from south coastal region of Karnataka. The *Borassus Flabellifer* husk is separated from the fruit using retting method. Polyester raisin is used as a matrix for composite preparation. Polyester resin is employed as a matrix material because it meets all the necessary requirements of a matrix while also being cost-effective. The extraction of fiber involves thoroughly washing the Borassus Flabellifer husk to remove all external particles. The fibers are then separated using the retting process, where the husk is soaked in water for 7 days. The water is regularly changed to prevent microbial growth and foul odor. This process loosens the fibers from the husk. The fibers are then manually extracted and dried at 70˚C for 24 hours[3].

Hand Layup Method

The production of composites used open metal molds measuring 300x200 mm. A thin layer of wax was applied to the molds to ensure easy removal of the composite after manufacturing. A predetermined amount of pre-cobalt ion treated polyester resin was mixed with methyl ethyl ketone peroxide (MEKPO), a hardener. Initially, a thin layer of the polyester resin matrix was coated as a primary layer onto the mold surface. To achieve a smooth and refined surface, a sheet of BFF was placed over the primary layer, followed by pouring and evenly distributing a secondary layer of the matrix along the corners of the mold. The fiber was inserted into the matrix within the mold. The composite was allowed to cure within the mold for 2 hours. The process is shown in fig 1. After curing, the composite was extracted from the mold and placed under weight for 24 hours. This process was repeated for variations in the fiber-matrix ratio

of 1:30, 1:40, 1:50, 1:60, and 1:70 [4]. The fabricated composites based on variations in fiber-matrix ratio are shown in fig 2.

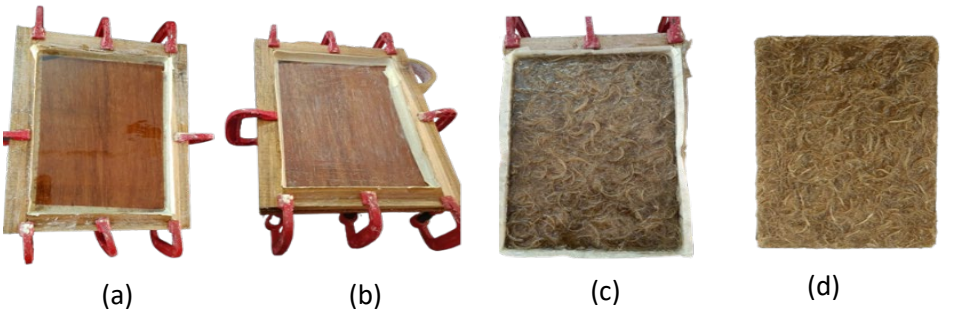

Fig 1. (a) wooden mold, (b) wax applied mold, (c) fiber-matrix layer placement, (d) fabricated composite

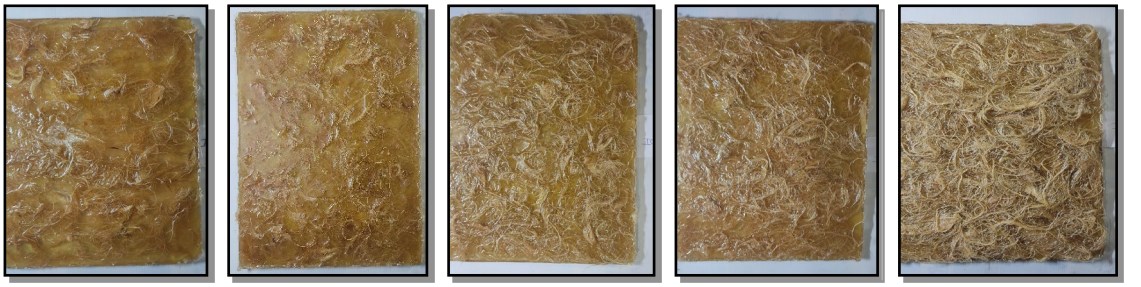

Fig 2. Different composites based on ratio of fiber and matrix (a) 1:70, (b) 1:60, (c) 1:50, (d) 1:40 and (e) 1:30

3 Results and Discussions

The fibers extracted from Borassus Flabellifer husk using the retting process are free from external particles and maintain structural integrity. The application of a primary resin layer followed by a BFF sheet and a secondary resin layer results in a smooth and uniform composite surface. The fibers are evenly distributed within the matrix, ensuring uniform mechanical properties throughout the composite. The 2-hour curing process is sufficient to achieve a well-cured composite with minimal internal stresses. The surface treatment of fibers results in a strong bond with the polyester resin matrix, enhancing the durability and indicating overall mechanical performance of the composites. The use of natural fibers significantly reduces the cost of composite materials compared to synthetic alternatives.

4 Conclusions

The *Borassus Flabellifer* fiber-matrix composite material possesses qualities like biodegradability, biocompatibility, and renewability. The use of biodegradable and renewable natural fibers lowers the environmental footprint of the composites, contributing to sustainability. The results suggest potential for further research into optimizing fiber treatments and exploring other natural fibers to enhance composite performance. These possible results provide a comprehensive overview of the outcomes expected from the fabrication process, highlighting key aspects of fiber quality, composite performance, and environmental impact.

References

1. B. Laycock, S. Pratt, P. Halley, A perspective on biodegradable polymer biocomposites - from processing to degradation, *Functional Composite Materials* **4**(1) 1-12 (2023), doi: 10.1186/S42252-023-00048-W.
2. M. Syduzzaman, M. A. Al Faruque, K. Bilisik, M. Naebe, Plant-based natural fibre reinforced composites: A review on fabrication, properties and applications, *MDPI AG* (2020), doi: 10.3390/coatings10100973.
3. G. Sunny, T. Palani Rajan, An effect of retting process and extraction methods on physical and mechanical properties of areca nut fibers, *International Journal of Clothing Science and Technology* 36(4) 722-739 (2024), doi: 10.1108/IJCST-09-2023-0133/FULL/XML.
4. G. Chethan, K. C. Sunil, Y. Narayana, Effect of Surface Modification on the Impact Strength and Hardness of Areca Husk Fibre Reinforced Polyester Resin Composite, *Materials Science Forum* **1082** 105–110 (2023), doi: 10.4028/P-31H8T9.

Assessment of the density *of Borassus flabellifer* Fruit Husk Fiber from southern part of Coastal Karnataka

Kavya G K, Chethan G, Mahantesh Bankapur and Narayana Y*
Department of Physics, Mangalore University, Mangalagangotri – 574199

* E-mail: narayanay@mangaloreuniversity.ac.in

Abstract

Natural fibers are increasingly valued for their sustainability and eco-friendly attributes, enhancing their appeal as reinforcements in composite materials. This study investigates the density of Borassus flabellifer fruit fibers (BFF) from South Coastal Karnataka, essential for evaluating their role as sustainable composite reinforcements. Extracted using the retting method to ensure purity, BFF exhibited densities ranging from 100 kg/m³ to 146.67 kg/m³ across various regions. Notably, BFF demonstrates the lowest density among commonly used natural fibers in composite production, making it highly advantageous for lightweight applications without compromising strength. This characteristic, coupled with BFF's biodegradability, underscores its potential for environmentally friendly composite materials. The findings contribute valuable insights into optimizing BFF's utilization in eco-conscious engineering applications, promoting sustainable practices in material science and composite technology. This study highlights the importance of natural fiber selection in achieving both performance and sustainability goals in composite material development, paving the way for greener innovations in engineering and industry.

Keywords: Natural fiber, lignocellulose fiber, degradable, natural fiber composite.

1 Introduction

The quest for sustainable materials in engineering has brought natural fibers into the spotlight due to their renewability, biodegradability, and environmental benefits compared to synthetic fibers [1]. Among these, *Borassus flabellifer,* or Ice apple fruit, is notable for its potential as a reinforcement material in composites. Sourced from the fruit husk of the Palmyra palm, which is commonly found in tropical regions like Southern Coastal Karnataka, India, this natural resource offers a promising opportunity for sustainable composite development [2]. A comprehensive understanding of BFF density is crucial for its effective use in composites. Density influences the weight,

strength, and durability of fiber-reinforced materials, making it essential for applications requiring lightweight, high-performance materials [3]. This study aims to assess the density of BFF from various South Coastal Karnataka regions to determine its suitability for composites. These advancements support sustainable practices in material science and composite technology, aligning with global efforts to reduce environmental impact and foster green innovation [4].

2 Materials and Methods

BFF were collected from various regions of South Coastal Karnataka and were extracted using the retting method, where the fruit husks were immersed in a solution to separate the fibers, followed by thorough washing and drying [5]. Figure 1A shows the collected fruit husk and Figure 1B displays the extracted fibers.

To determine the density of the fibers, they were finely chopped for uniform packing. A container of known volume was weighed empty, then filled with the chopped fibers, and the total mass was recorded. The density was calculated using the formula:

$$\text{Density} = \frac{M_f - M_c}{V_c}$$

where M_c is the mass of the empty container, M_f is the mass of the container filled with BFF, and V_c is the volume of the container. This method ensures accurate measurement of fiber density by directly relating the mass of the fibers to the known volume of the container.

A B

Fig 1. A. Collected fruit husk. B. Extracted fibers from the husk.

3 Results and Discussions

The density values of BFF from South Coastal Karnataka, as shown in Table 1, range from 100.00 kg/m³ to 146.67 kg/m³. Notably, BFF exhibits a lower density compared to other commonly used natural fibers. For instance, jute fibers have a density of

approximately 1200 kg/m³ [6], while flax fibers are reported to have a density around 1600 kg/m³ [7]. This low density of BFF makes it particularly advantageous for lightweight composite applications, aligning with the growing demand for eco-friendly materials in sustainable engineering solutions [8].

Table 1: Density of BFF from various regions of South Coastal Karnataka

Area	Density (kg/m³)
Mangalore	126.67
Kapu	113.33
Someshwara	146.67
Moodbidri	113.33
BC Road	100.00
Kasaragod	140.00
Hosmar	120.00
Dharmasthala	113.33
Puttur	133.33

4 Conclusion

This study has examined the density of BFF from various regions of South Coastal Karnataka, revealing a range from 100 kg/m³ to 146.67 kg/m³. The findings indicate significant regional variation, influenced by local environmental factors and fiber preparation methods. The relatively low density of BFF makes it a promising candidate for lightweight composite materials, offering potential benefits in applications where weight reduction is crucial. These insights highlight the value of BFF as a sustainable reinforcement material and suggest that further research could optimize its use in diverse engineering applications.

References

1. O. Faruk, A. K. Bledzki, H.-P. Fink, M. Sain, Biocomposites reinforced with natural fibers: A review, *Progress in Polymer Science* **39**(4) 662-680 (2014), doi: 10.1016/j.progpolymsci.2013.11.002
2. N. Reddy, Y. Yang, Preparation and characterization of natural fiber-reinforced polymer composites, *Journal of Composite Materials* **39**(5) 421-435 (2005) doi: 10.1177/0021998305044967.

3. M. Amel, M. Bousmina, A. Zarrouk, The effect of density on the mechanical properties of natural fiber reinforced composites: A review, *Composites Part A: Applied Science and Manufacturing* **110** 34-42 (2018), doi: 10.1016/j.compositesa.2018.04.021.
4. K. L. Pickering, M. G. A. Efendy, T. M. Le, A review of recent developments in natural fiber composites and their mechanical performance, *Composites Part A: Applied Science and Manufacturing* **83** 98-112 (2016), doi: 10.1016/j.compositasa.2015.08.038.
5. H. Wang, H. Zhang, Z. Wang, Effect of retting methods on the properties of natural fibers and their application in composites, *Journal of Cleaner Production* **279** 123715 (2021) doi: 10.1016/j.jclepro.2020.123715.
6. S. Jain, R. Yadav, N. Sharma, Recent developments in jute fiber reinforced composites: A review, *Journal of Composite Materials* **54**(18) 2655-2681 (2020), doi: 10.1177/0021998320904536.
7. M. S. Huda, Y. Zhang, K. Muthukumarappan, Properties of flax fibers and their use in composite materials: A review, *Journal of Natural Fibers* **18**(3) 335-355 (2021), doi: 10.1080/15440478.2020.1727545.
8. M. J. John, S. Thomas (2008), Biofibres and biocomposites, *Carbohydrate Polymers* **71**(3) 343-364 (2008), doi: 10.1016/j.carbpol.2007.05.040.

Structural and electrical characterization of degenerate semiconductor thin films of CdZnO obtained using the spray pyrolysis technique

E Deepak D'Silva*, Anagha A, Akash Arjun Bag, Sandra Sajeevan

Department of Post graduate Studies & Research in Physics, St Aloysius (Deemed to be University), Mangaluru, 575003, Karnataka, India

* E-mail: deepak.dsilva@gmail.com

Abstract

Pure and zinc-doped CdO (1, 3, 5, 10, and 15 wt % of Zn) thin films were synthesized through the spray pyrolysis technique on the glass substrate. The structural, and electrical studies of the thin films were carried out. The powdered XRD analysis revealed that the deposited thin films are face-centered cubic structures of monteponite CdO. The electrical characteristics obtained by using Van der Pauw Hall effect measurements showed a noticeable decrease in the electrical resistivity of the films with increasing concentrations of zinc doping, which made them exhibit advantageous degenerate semiconductor property.

Keywords: TCO, degenerate semiconductor, Powder XRD, Van der Pauw Hall effect.

1 Introduction

A "degenerate thin film" typically refers to a thin film made of a material in which the electrons are in a state of degeneracy. Degeneracy is a situation where multiple quantum states of a system have the same energy. In the case of materials, this often occurs when the electron density is very high, such as in metals or highly doped semiconductors, where the fermi energy level is close to the energies of the available electronic states. So, there is always a need for new thin film materials with excellent properties for device applications, which depend upon the growth conditions, surface morphology, particle size and shape, and bandgap variation [1, 2].

In our study, we have investigated CdZnO thin films using the spray pyrolysis technique, focusing on modifying two critical parameters: the spray rate and the distance from the nozzle to the substrate. Our analysis revealed that the resultant thin films exhibited characteristics indicative of degenerate semiconductor behavior. Specifically, the deposited films showcase properties conducive to electrically conductive applications. This highlights the potential of our tailored approach to optimizing spray pyrolysis parameters in enhancing the functionality of CdZnO thin films.

2 Experimental Techniques

Pure CdO and Zn-doped CdO thin films with 0, 1, 3, 5, 10, and 15 wt. % of Zinc were prepared using the spray pyrolysis technique on glass substrates at 350°C. A standardized solution at a concentration of 0.1M was prepared by dissolving cadmium acetate in distilled water. To prepare the doped films, a 0.1 M solution of zinc acetate was added to the precursor solution, which was then directly sprayed onto the substrate. The glass substrates were thoroughly cleaned and dried prior to deposition. The formation of the nanostructured $Cd_{1-x}Zn_xO$ films is observed after the chemical reaction.

$$\begin{matrix} Cd(CH_3COO)_2.2H_2O \\ + \\ Zn(CH_3COO)_2.2H_2O \end{matrix} \xrightarrow[\text{Decompose}]{350\ ^oC} CdZnO\downarrow + CO_2\uparrow + CH_4\uparrow + \text{Steam}$$

At the end of the chemical reaction, a yellow-colored deposition of pure CdO film is obtained, and all the prepared doped $Cd_{1-x}Zn_xO$ films were dark yellowish. The prepared thin films were annealed in a hot air oven at 350 °C to remove any other organic residues in the solutions. The structural properties of the thin films were measured by the powder-XRD (Bruker) using Cu-Kα radiation (λ = 1.5406 Å). Hall coefficient, mobility and carrier concentration were quantified by Van der Pauw technique.

3 Results and Discussions

Powder XRD analysis

Figure 1 depicts the X-ray diffraction patterns of thin films of CdO and Zn-doped CdO. XRD measurements were conducted using Cu-Kα radiation (λ = 1.5406 Å) within the 2θ range of 20 to 80 degrees. The sharpness of the XRD peaks suggests that the films possess a crystalline structure. The samples are the face-centred cubic structure of monteponite CdO. It was observed that the crystal structures of the films remained unchanged with Zn doping [3]. The 2θ values corresponding to the (1 1 1), (2 0 0), and (2 2 0) peaks of pure CdO were measured as 33.75°, 39.0°, and 55.9°, respectively. The absence of Zn-related peaks in the CdO:Zn thin films confirms homogeneous dispersion of dopants within the CdO lattice, preserving its cubic structure [3, 4]. Moreover, the 2θ position of the pure CdO peaks slightly shifts towards higher angles with Zn doping, indicating lattice contraction. This contraction arises from the substitution of smaller Zn^{2+} ions (0.71 Å) for Cd^{2+} ions (0.97 Å) in the CdO lattice. From the wavelength (λ) of the CuKα radiation, the full-width half-maximum of the diffraction peak (β), lattice constant (a), diffraction angle (θ); the crystallite size (D), microstrain (ε), dislocation density (δ), interplanar distance d, lattice constant a and

unit cell volume V values of the CdO, and CdO:Zn thin films were estimated from the formulae [5] and presented in Table 1.

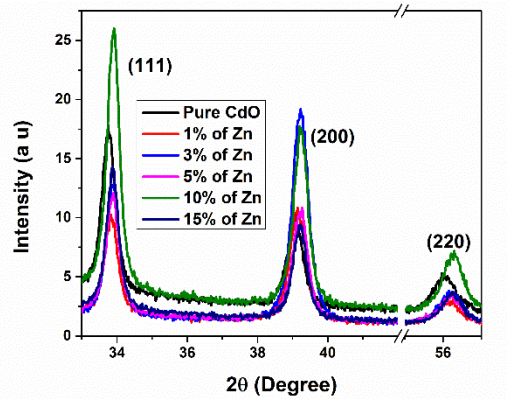

Fig. 1 Powder XRD pattern of pure and Zn doped CdO thin films

Electrical studies

The electrical characteristics of zinc-doped cadmium oxide (CdO) thin films were thoroughly examined using Van der Pauw Hall effect measurements. Prior research [6] indicates that pristine CdO films typically exhibit n-type conductivity. Various parameters, such as electrical resistivity, carrier density, Hall coefficient, and Hall mobility, were meticulously measured, analyzed, and tabulated in Table 2. A conspicuous decrease in the electrical resistivity of the films was observed with increasing concentrations of zinc doping. This decline can be attributed to the amelioration in crystallite quality, resulting in a more ordered lattice structure. As crystallite size amplifies, atomic arrangements within the lattice become more organized, thereby diminishing grain boundaries and consequently enhancing conductivity. The collective effects, encompassing improved crystallite quality, reduced scattering, and heightened carrier density, collectively contribute to the augmentation of the electrical properties of the thin films, rendering them akin to degenerate semiconductors. Such characteristics are pivotal for applications such as solar cells, transistors, sensors, and display panels.

Table 1: XRD analysis of CdO and Zn doped CdO

Doping concentration of zinc (%)	(hkl)	2θ	FWHM degree	D (nm)	D (nm)	$\delta = \frac{1}{D^2}$ $\times(10^{15}/m^2)$	$\varepsilon = \beta cos\theta/4$ $\times(10^{-3})$	d (A)	a (A)	V $(A)^3$
0%	(111)	33.75	0.5689	15.2296	15.2560	4.3114	2.3757	2.6536	4.596	97.1
	(200)	39.1	0.5757	15.2824		4.2816	2.3674	2.3019	4.603	97.6
1%	(111)	33.84	0.5596	15.4866	15.5723	4.1695	2.3362	2.6467	4.584	96.3
	(200)	39.14	0.5620	15.6580		4.0787	2.3106	2.2996	4.599	97.3
3%	(111)	33.91	0.5297	16.3634	15.8399	3.7346	2.2110	2.6414	4.575	95.8
	(200)	39.22	0.5747	15.3163		4.2627	2.3622	2.2951	4.590	96.7
5%	(111)	33.87	0.5283	16.4056	16.6237	3.7154	2.2053	2.6444	4.580	96.1
	(200)	39.27	0.5227	16.8417		3.5255	2.1482	2.2923	4.584	96.4
10%	(111)	33.89	0.4872	17.7901	18.1456	3.1596	2.0337	2.6429	4.577	95.9
	(200)	39.2	0.4757	18.5011		2.9214	1.9556	2.2963	4.592	96.9
15%	(111)	33.87	0.5007	17.3116	17.4915	3.3367	2.0899	2.6444	4.580	96.1
	(200)	39.22	0.4981	17.6713		3.2022	2.0474	2.2951	4.590	96.7

Table 2: Electrical parameters of Zn doped CdO thin films

Sample	**Thickness** t (nm)	**Resistivity** ρ (Ω cm)	**Hall Coefficient** R_H (cm^3/C)	**Carrier Mobility** μ (cm^2/V.s)	**Carrier density** n (/cm^3)
Pure CdO	580	3.79×10^{-2}	-0.099	24922.9	0.627×10^{20}
CdZnO(1%)	600	1.03×10^{-3}	-0.05	4854.5	1.25×10^{20}
CdZnO(3%)	650	6.64×10^{-4}	-0.03	80.4	2.05×10^{20}
CdZnO(5%)	700	5.03×10^{-4}	-0.028	4343.1	2.17×10^{20}
CdZnO(10%)	780	3.99×10^{-4}	-0.02	14671.4	3.04×10^{20}
CdZnO(15%)	860	1.40×10^{-4}	-0.002	397.1	31.3×10^{20}

4 Conclusions

Pure and Zn-doped CdO structures were synthesized using the spray pyrolysis method. The XRD patterns of all the thin film samples found the face-centered cubic structure of monteponite CdO, and no impurity phase was observed. The electrical studies reveal that doping makes the thin films degenerate semiconductors, which have many practical applications and can be used as a potential candidate for opto-electronic device applications.

References

1) D. A. Granada-Ramírez, A. Pulzara-Mora, C. A. Pulzara-Mora, A. Pardo-Sierra, J. A. Cardona-Bedoya, M. Pérez-González, S. A. Tomás, S. Gallardo-Hernández, J. G. Mendoza-Álvarez, *Applied Surface Science* **586** 152795 (2022)
2) Z. Ghorannevis, M. T. Hosseinnejad, M. Habibi & P. Golmahdi, *J Theor Appl Phys* **9** (2015)
3) B. Amudhavalli, R. Mariappan, M. Prasath, *Journal of Alloys and Compounds* **925** 166511 (2022)
4) K. Usharani, A. R. Balu, *Acta Metallurgica Sinica (English Letters)* **28** 1 (2015)
5) V. K. Ashith, E. Deepak D'Silva, *J Mater Sci: Mater Electron* **32** 10028–10048 (2021)
6) P. Velusamy, R. Ramesh Babu, K. Ramamurthi, E. Elangovan, J. Viegas, M. Sridharan, *Sensors and Actuators B: Chemical* **255** 1 (2018)

Green Reduction of Graphene Oxide using Averrhoa Carambola

Alog S Kumar[1] *, Sandra C Umesh[1], Kumara K[2]

[1] *Department of Post Graduate Studies & Research in Physics, St Aloysius (Deemed to be Univerity), Mangalore-575003, Karnataka.*

[2]*Department of Physics, M.P.E Society's S.D.M Degree College, Honnavar, 581334, Karnataka.*

*Email: alogakku123@gmail.com

Abstract

We synthesized graphene oxide (GO) using the Modified Hummers method and subsequently reduced it using a novel approach employing the green reducing agent Averrhoa Carambola (Star fruit). The structural and optical properties of the reduced graphene oxide (rGO) were analyzed using X-ray diffraction (XRD), Fourier-transform infrared spectroscopy (FTIR), and UV-Vis spectroscopy.

Keywords: Synthesis, Graphene Oxide, Reduced Graphene Oxide, Averrhoa Carambola (Star fruit extract)

1 Introduction

Reduced Graphene Oxide (rGO) is derived from graphene oxide (GO) through a reduction process that removes oxygen-containing functional groups, restoring the sp^2 carbon structure. This reduction enhances rGO's optical, electrical conductivity and mechanical properties compared to GO. rGO finds applications in various fields including electronics, energy storage, sensors, and biomedical devices, owing to its excellent conductivity, high surface area, and chemical stability [1,2,3] . Its synthesis typically involves methods such as chemical reduction with agents like hydrazine or green reducing agents to minimize environmental impact [1,4]. While some green reducing agents like plant extracts have been explored, their efficiency and scalability for large-scale production need further investigation. Developing sustainable reduction methods that minimize environmental impact remains a research gap.

2 Materials and Methods/Model

Graphite powder was reduced to Graphene Oxide using Modified Hummer's Method [3]. GO reduced to rGO using a green reducing agent named Averrhoa Carambola (Star Fruit Extract). Star fruit was washed with distilled water, cut into small pieces

and is added into a beaker containing distilled water (100ml). The solution was boiled for 30 min and kept for cooling and filtered using filter paper. The Graphene powder (10 mg) was added to a beaker containing Star fruit extract (100 ml) and ultrasonicated for 2 hours. The solution had stirred at 500 rpm using a magnetic stirrer. Stirring time was kept for 40 h in 60°C. The obtained rGO gets dispersed in ethanol homogeneously.

3 Results and Discussion

Figure 1 presents the X-ray diffraction patterns for graphite, GO, and rGO. In Figure 1a, a high-intensity peak around 10 degrees is observed, corresponding to the (001) plane of graphene oxide (GO), confirming its presence. This peak signifies an expanded interlayer spacing relative to pristine graphite, attributable to the oxygen-containing functional groups (hydroxyl, carboxyl, and epoxy) present on the graphene sheets. In Figure 1b, for rGO, the prominent peak at 26.5 degrees suggests that van der Waals forces have partially restored the graphitic structure.

Figure 2 shows Fourier transform infrared spectra of GO and rGO. In GO, there is broad peak approximately 3270 cm^{-1} in GO spectrum because of hydroxyl groups presence, which shows moisture absorption and oxygen-containing moieties like carboxylic, carbonyl, hydroxyl and epoxy. This peak can be also found in star fruit reduced rGO spectrum with relatively lower intensity, which shows

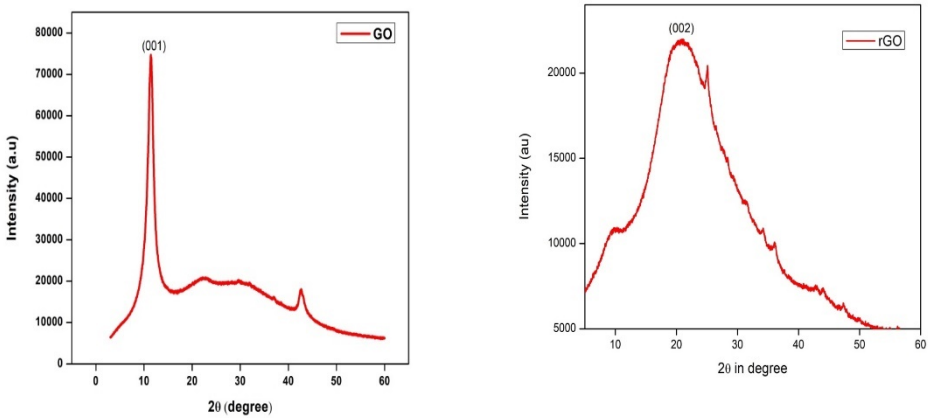

Fig. 1 (a) XRD pattern of GO; (b) XRD pattern of rGO

that hydroxyl groups has partially been removed (Figure 2b). Intensities of peaks for C=O stretching at 1625 cm^{-1} shows it is partially reduced (Intensity peaks of C=O in GO is around 1730 cm^{-1}). The C-OH stretching around 1216 cm^{-1}, and C-O stretching vibration around 1041 cm^{-1} in the rGO spectrum were not reduced. The peaks which

corresponds to C=O in aromatic rings has shifted from 1720cm^{-1} to 1625 cm^{-1} indicates partial reduction of GO [4].

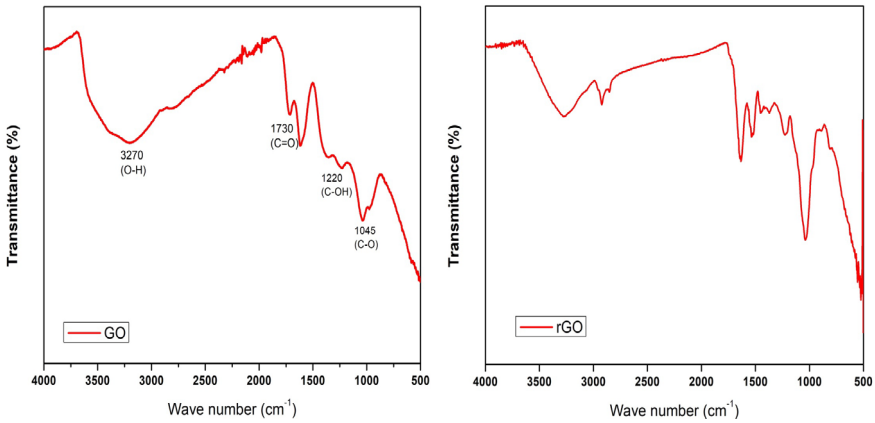

Fig. 2 FTIR spectra of (a) GO and (b) Rgo

Figure 3 displays the UV-Vis spectrum of rGO, which reveals a redshifted absorption peak at 268 nm. This shift indicates the successful removal of oxygen functional groups through reduction and the restoration of π-conjugation within the graphene sheets [1].

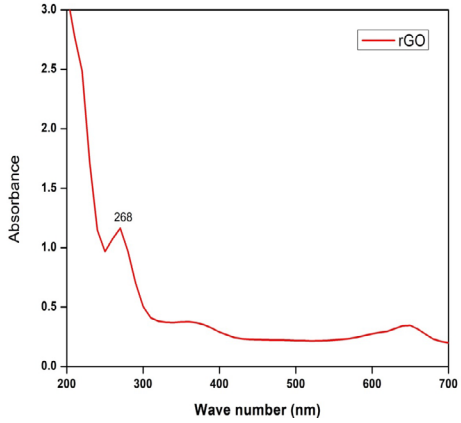

Fig. 3 UV-Vis spectrum of rGO

4 Conclusions

We prepared GO from graphite powder using the Modified Hummer's Method and reduced it with Averrhoa Carambola. This reduction resulted in selective and partial reduction of rGO, as not all oxygen-containing functional groups were removed.

Consequently, while Averrhoa Carambola may not be the best green reductant for complete reduction of graphene oxide, it can be useful for selective reduction. Adjusting the concentration of the reducing agent could potentially achieve full reduction of rGO.

References

1. M. Zhou, Y. Zhai, S. Dong, Electrochemical sensing and biosensing platform based on chemically reduced graphene oxide, *Analytical Chemistry* **81** 5603–5613 (2009)
2. J. Wang, E. C. Salihi, L. Šiller, Green reduction of graphene oxide using alanine, *Mater. Sci. Eng. C* **72** 1-6 (2017)
3. A. L. Patterson, The Scherrer formula for x-ray particle size determination, Phys. Rev. **56**(10) 978–982 (1939)
4. Characterisation of reduced graphene oxide: Effects of reduction variables on electrical conductivity, *Mater. Sci. Eng. B* **193** 49–60 (2015)

Reduced Graphene Oxide Optimization and its Influence on the Optoelectronic Behaviour of Gallium-Doped Zinc Oxide

Amulya Rai[1*], Rashmi N[2], Felcy Jyothi Serrao[2], Kumara K[3]
[1]*Department of PG Studies and Research in Physics, St. Aloysius (Deemed to be University), Mangalore 575003, Karnataka, India*
[2]*Department of Physics, Sahyadri College of Engineering & Management (Autonomous), Mangaluru 575007, Karnataka, India*
[3]*Department of Physics, M.P.E Society's S.D.M. Degree College, Honnavar, 581334, India*

[*]Email: raiamulya05@gmail.com

Abstract

Thin films of Gallium-doped Zinc Oxide (GZO) with dopant percentages of 1%, 3%, and 5%, and varying amounts of reduced graphene oxide (r-GO) (0.001g, 0.003g, 0.005g) were deposited onto glass substrates using the spin coating method. The structural, optical, and electrical properties of these films were analyzed through X-ray diffraction (XRD), UV-Visible spectroscopy, and two-probe techniques. An additional graphitic carbon nitride peak was observed in all rGZO samples, possibly causing shifts in ZnO peaks. Interplanar distances in the films remained consistent across all samples. Film properties were significantly influenced by strain, dislocation density, and particle size, which were increased with r-GO addition.

Key words: Optimization, Crystallinity, Band gap, Transparency

1. Introduction

Transparent conducting oxides (TCOs) are essential for various optoelectronic devices due to their unique properties: high conductivity, optical transparency, infrared reflectivity, and heating efficiency. Widely used in displays, solar cells, and sensors, ITO has been the standard TCO. However, due to its limitations, researchers explore alternatives like graphene, carbon nanotubes, conducting polymers, metal nanowires, and hybrid structures to enhance performance and address challenges in optoelectronics [1-2]. Zinc oxide (ZnO) is a promising, cost-effective TCO alternative to ITO and FTO. However, pure ZnO is highly resistive. To enhance conductivity, it requires doping with elements like Al or Ga. This doping introduces shallow donor states, increasing carrier concentration and reducing resistivity, making ZnO suitable for TCO applications [3-4]. In this work, a spin coater was utilized to create a series of composite thin films of gallium doped zinc oxide/rGO and examined the films' structural, electrical, and optical characteristics using an X-ray detector, two probes, and a UV-visible spectrophotometer.

2. Materials and Methods

GZO sol was prepared by dissolving zinc acetate dihydrate (99.99% purity) in 2-methoxyethanol with monoethanolamine (MEA) as a stabilizer, maintaining a 1:1 molar ratio and a total concentration of 0.5 mol/L. Gallium dopant was added at 1.0 at.% relative to Zn. The solution was stirred at 50°C for 1 hour and incubated at room temperature for 2 days. GZO sols were made with Ga concentrations of 1%, 3%, and 5%. r-GO powder was mixed with 5 mL of 2-methoxyethanol and sonicated for 1 hour, with r-GO amounts of 0.001 g, 0.003 g, and 0.005 g. Then, 5 mL of GZO sol was added to the r-GO sol and sonicated for 1 hour.

The glass substrates were cleaned and films were deposited at room temperature using a spin coater at 3000 rpm for 30 seconds. The films were preheated at 350°C for 15 minutes to evaporate solvents and remove residues, then annealed at 500°C in air for one hour. A total of 12 films were made: three for each gallium doping level with three r-GO amounts, plus three additional GZO films without r-GO. Each film had a thickness of approximately 7 to 8 layers.

3. Results and Discussion

X-ray diffraction (XRD) analysis confirmed the presence of ZnO, r-GO, GO and Ga peaks at specific angles. Additionally, a graphitic carbon nitride peak was consistently observed in all rGZO films, which potentially caused the shifts in ZnO peaks. The interplanar distances within the crystal lattice of the thin films were found to be nearly identical across all samples, consistent with Bragg's law. In rGZO films, there is a noticeable rise in both film strain and dislocation density compared to films without rGO. Additionally, particle sizes in rGZO films increased proportionally with higher rGO content [5-6].

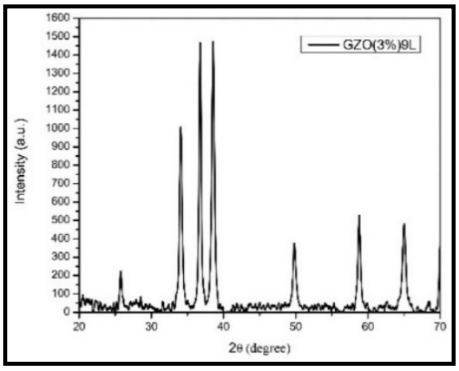

Fig. 1 XRD pattern of 3% GZO film

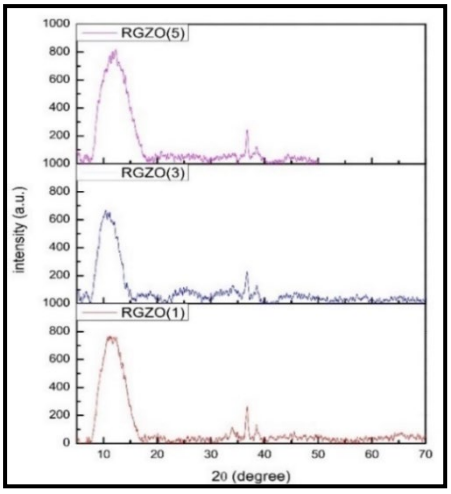

Fig. 2 XRD patterns of 3% RGZO films

Table 1: Structural properties of GZO and GZO films

Film	FWHM (β)	Crystallite Size (D) $x10^{-8}$	Film Strain $x10^{-3}$	Dislocation Density (δ)	Interplanar spacing (d)	Lattice constant (c) $x10^{-10}$
GZO(3%)	0.00819	1.7929	1.93	$3.11x10^{15}$	$2.331x10^{-10}$	4.662
RGZO(3%,.1)	0.0113	1.2929	2.68	$5.98x10^{15}$	$2.445x10^{-10}$	4.89
RGZO(3%,.3)	0.0134	1.0904	3.17	$8.41x10^{15}$	$2.445x10^{-10}$	4.89
RGZO(3%,.5)	0.00942	1.55	2.23	$4.16x10^{15}$	$2.440x10^{-10}$	4.88

In the visible range, the films showed an average transmittance of up to 80%. The films' optical transparency has increased as a result of the incorporation of rGO, while their optical band gaps have shrunk. The addition of rGO increases the number of rGO flakes on the film's surface, improving light absorption. Larger crystallite sizes resulted in increased Urbach energies, was evident in 3% rGZO films, indicating greater disorder in the films. The particle size increase in 3% Ga-doped ZnO and rGZO films corresponded to reduced energy band gaps [7].

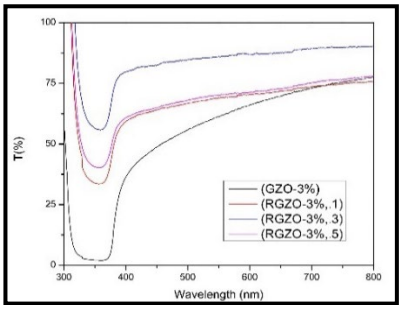

Fig. 3 Transmittance spectra of 3% GZO and RGZO films with varying rGO concentration

When rGO is added to a film, the resistivity of the rGZO film decreases relative to the GZO film. This suggests that the rGO-containing thin film has higher conductivity, supporting the idea that rGO increases a film's conductivity. This can be explained by graphene's bipolar structure, which allows for the almost instantaneous flow of electrons and holes and an increase in carrier concentration.

Table 2: Crystallite size, energy gap and Transmittance value of Thin films

Film	Crystallite Size (D)	Energy band gap (E_g)(eV)	Urbach Energies	Refractive index (R.I.)	Transmittance
GZO(3%)	$1.7929x10^{-8}$	3.23	1.24	0.96	61%
RGZO(3%,.1)	$1.2929x10^{-8}$	3.17	0.287	0.04	68%
RGZO(3%,.3)	$1.0904x10^{-8}$	3.19	0.1804	0.026	86%
RGZO(3%,.5)	$1.55x10^{-8}$	3.14	0.3387	0.037	70%

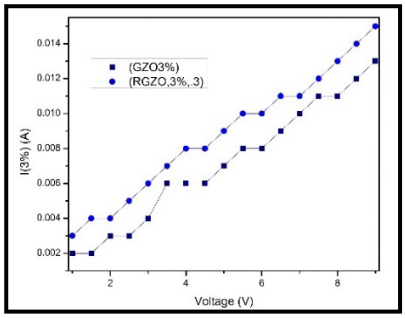

Fig. 4 I-V plot of 3% GZO and RGZO films

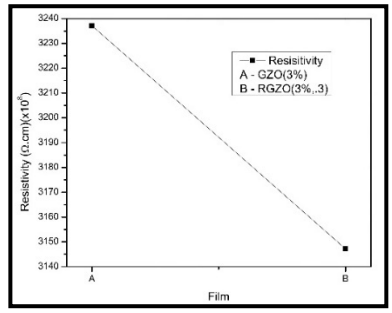

Fig. 5 Resistivity plot of 3% GZO and RGZO films

The involvement of intrinsic defects, also known as native defects, which are a product of the growth circumstances and impurity atoms of the ZnO particles under study, may be responsible for the enhanced conductivity of thin films. Moreover, ZnO-rGO is an insulator-semiconductor nanocomposite in which ZnO nanoparticles are affixed to the insulating rGO sheets' surface.

4. Conclusions

XRD analysis confirmed the hexagonal wurtzite structure of ZnO with a preferential c-axis orientation. The incorporation of rGO led to reduced grain size, increased strain, and dislocation density in the ZnO films. Despite this, the films maintained high transparency with improved light absorption due to increased rGO flakes. The addition of rGO significantly enhanced the conductivity of the films, likely due to graphene's bipolar structure and increased carrier concentration. However, the presence of localized states caused fluctuations in optical properties. The study suggests that ZnO-rGO nanocomposites with tailored properties can be achieved by controlling rGO content, offering potential applications in optoelectronic devices.

References:

1. N. S. A. Aziz et al., *Sains Malaysiana* **46**(7) 1083–1088 (2017)
2. S. D. Ponja et al., *Sci. Rep.***10**(1) 1–7 (2020)
3. M. A. Gross et al., *Mater. Res. Express* **6**(9) (2019)
4. J. Beckford et al., *AIP Adv.* **11**(7) 1–7 (2021)
5. Q. Qiao et al., *Optoelectron. Adv. Mater. Rapid Commun.* **4**(8) 1144–1148 (2010)
6. Y. Caglar et al., *Eur. Phys. J. B* **58**(3) 251–256 (2007)
7. V. S. Kindalkar et al., *Mater. Res. Express* **6**(9) (2019)

Al Doping Effects on Structural, Optical, and Electrical Properties of Sol-gel Derived rGO-AZO Nanocomposite Thin Films

Rashmi N[1*], Amulya Rai[2], F. J. Serrao[3], K.Kumara[4], N.B. Rithin Kumar[5]

[1]*Research Centre, Department of Physics, Sahyadri College of Engineering & Management (Autonomous), Mangaluru 575 007, Karnataka, INDIA (Affiliated to Visvesvaraya Technological University "Jnana sangama" Belagavi-5900018) INDIA.*

[2]*Department of Physics, St Aloysius (Deemed to be University), Mangaluru 575 003, Karnataka, INDIA.*

[3]*Department of Physics, Sahyadri College of Engineering & Management (Autonomous), Mangaluru 575 007, Karnataka, INDIA.*

[4]*Department of Physics, M.P.E Society's S.D.M. College, Honavar, INDIA.*

[5]*Department of Physics, A J Institute of Engineering and Technology, Mangaluru 575006, Karnataka, INDIA.*

*Email: rashminekkarla@gmail.com

Abstract

Transparent conductive Aluminum doped zinc oxide and reduced graphene oxide rGO: AZO nanocomposite thin films were prepared by sol-gel spin-coating technique on a glass substrate. XRD results revealed the polycrystalline nature of the films with a hexagonal (wurtzite) crystal structure and a preferred orientation along c-axis consistent with pure ZnO. The presence of rGO did not alter the crystallinity ZnO. However, increasing Al doping led to a decrease in the intensity of the (002) plane, due to dopant segregation at grain boundaries and strain effects from Zn and Al ionic radius mismatch. Concurrently, the crystallite size of the composite films decreased from 25 nm to 10 nm with increasing Al content. AFM showed uniform nanoparticles with reduced grain size on increased doping. The films exhibited high optical transmittance (>82%) and decreased band gaps (3.28-3.08 eV), attributed to band edge bending. The electrical resistivity of the composite films was reduced by increasing the Al concentration making them suitable for transparent conducting electrodes in optoelectronic devices.

Keywords: Metal oxides, Doping, AZO thin films, Reduced graphene oxide, Nanocomposites.

1 Introduction

Metal oxide nanoparticles have unique properties due to their nanoscale dimensions, differing from their bulk forms. ZnO in particular, is a promising alternative to the commonly used transparent conducting oxide (TCO) ITO in optoelectronics. ZnO is an abundant, stable, non-toxic material with a large exciton binding energy of about 60 meV and a direct energy band gap of 3.37 eV [1]. Due to their doping ability, that enables improved and controlled properties, ZnO thin films are adaptable in modern

technology [2]. Dopants like aluminum (Al), gallium (Ga) and indium (In) from Group III are used to enhance its optical and electrical properties[3]. Additionally, the integration of reduced graphene oxide (rGO) with ZnO can result in heterostructures that greatly improve optoelectronic device performance [4]. In this work, rGO: AZO nanocomposite thin films were prepared by sol-gel spin coating method. The influence of Al concentration on the structural, optical and electrical properties of rGO: AZO composite films has been investigated.

2 Materials and Methods

2.1 Preparation and characterization of rGO: AZO composite thin films

Graphene oxide (GO) was prepared using a modified Hummer's approach, involving the addition of graphite flakes to conc. H_2SO_4 and $KMnO_4$, followed by sequential additions of deionized water and hydrogen peroxide, with subsequent washing and drying. rGO was obtained by mixing GO with ascorbic acid, ultrasonication, addition of hydrogen peroxide and further washing and drying. AZO sol was made by dissolving 0.5M Zinc acetate dihydrate and Aluminium nitrate nonahydrate in 2-methoxyethanol, with Monoethanolamine stirred at 40°C, and aged for 48 hours. In order to make rGO: AZO nanocomposite thin film, dry rGO was added to prepared AZO solution and ultrasonicated, then spin-coated onto cleaned glass substrates, preheated, and subjected to multiple spin-bake processes and post-heating to achieve high-quality films. The effects of Al concentration on the structural, morphological, optical, and electrical properties of the rGO: AZO composite thin films were investigated by XRD, UV-Vis spectroscopy, AFM and the Two Probe Method.

3 Results and Discussion

3.1 Structural properties

Fig. 2 shows the XRD patterns of rGO: AZO films at different Al concentrations. The films exhibited polycrystalline nature with a hexagonal crystal structure and c-axis orientation, similar to pure ZnO[5]. The inclusion of rGO did not alter the crystallinity or preferred orientation of ZnO, but the peak intensity decreased from pure ZnO to rGO:1wt% AZO, likely due to rGO functionalization by ZnO[6-8]. Increasing the Al dopant level further reduced crystallinity from 21 nm to 10 nm, possibly due to dopant segregation and strain effects from ionic radius mismatch between Zn and Al are summarized in Table 1. According to AFM study, surface roughness of the films decreased from 18.268 nm to 5.318nm, when the doping level was increased. These results are in agreement with the XRD results.

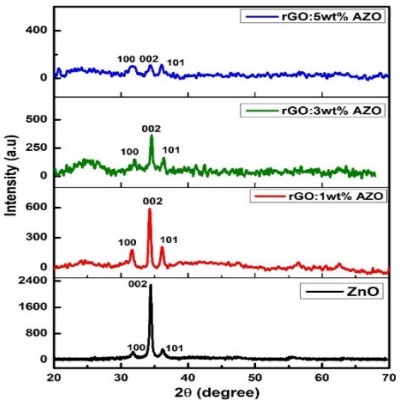

Fig. 1 XRD patterns of pure ZnO and composite films.

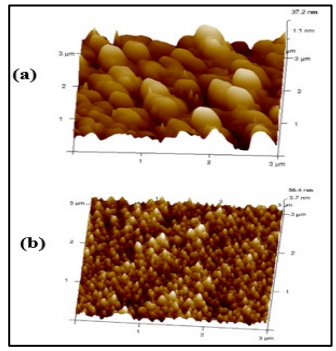

Fig. 2 AFM patterns of (a)pure ZnO and (b)rGO: AZO composite films.

Table 1. Structural and optical parameters of pure ZnO and rGO: AZO composite films

Samples	2θ (°)	FWHM (°)	D (nm)	δ (10^{15})	Transmittance %	Bandgap (eV)	E_U (meV)
ZnO	34.45	0.33	25.15	1.58	91%	3.23	126
rGO:1wt%AZO	34.28	0.37	21.48	2.16	94%	3.19	131
rGO:3wt%AZO	34.57	0.40	20.73	2.32	82%	3.14	218
rGO:5wt%AZO	34.39	0.90	9.211	11.7	90%	3.08	216

3.2 Optical properties:

Optical transmittance spectra of pure ZnO and rGO: AZO composite thin films at different Al concentrations in the wavelength range from 300 to 800 nm are shown in Fig.3(a). The films exhibited high optical transmittance (>82%). The decrease in the transparency of rGO: AZO thin films is observed with the addition of Al. The band gap decreases from 3.28 to 3.08 eV as Al concentration increases, due to band edge bending and additional impurity levels. The Urbach energy which reflects the disorder in the film network found to vary inversely with optical band gap. The rGO: AZO films with 3wt.% Al content show higher E_U values confirming the enhanced structural disorder and declined stoichiometry.

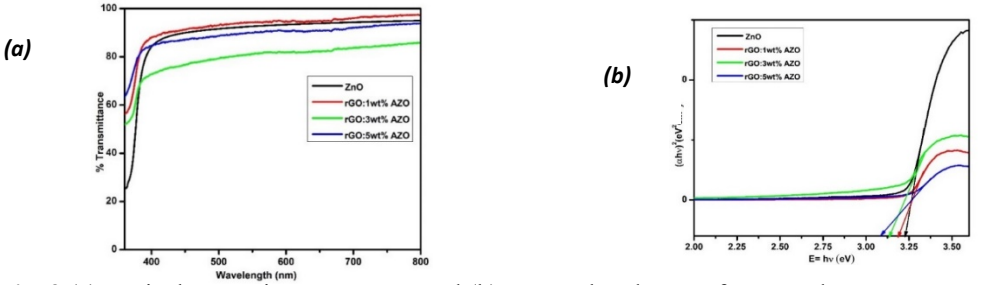

Fig. 3 (a) Optical transmittance spectra and (b) Energy band gaps of ZnO and rGO: AZO nanocomposite thin films.

3.3 Electrical properties:

The (I-V) study was performed using the two-probe method to investigate the electrical properties composite thin films. The films have good ohmic contact behaviour, as indicated by their linear I-V curves. The variation of electrical resistivity of rGO: AZO films at different Al doping concentrations are shown in Fig. 4. It was observed that electrical resistivity of the nanocomposite films reduced with increasing the Al concentration. Thus, the results are in agreement with the previous results observed in the literature [8].

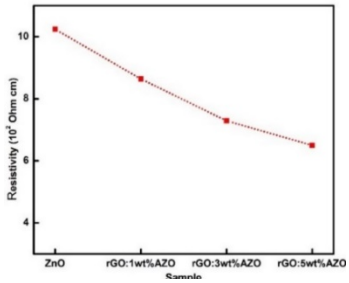

Fig. 4 The resistivity of pure ZnO and rGO: AZO composite films.

4 Conclusion

The presence of rGO did not alter the crystallinity of ZnO. The electrical resistivity of the composite films was reduced by increasing the Al doping making them suitable for transparent conducting electrodes in optoelectronic applications.

Acknowledgements

The authors are grateful to VGST for funding the UV-Visible Spectrophotometer at the Department of Physics, Sahyadri College of Engineering & Management. They also thank the Department of Physics, St. Aloysius (Deemed to be University), Mangaluru, for providing the XRD characterization facility.

References

1. T. Amakali et al., *Crystals*, **10**(2) 132 (2020)
2. M. Parashar et al., *J. Mater. Sci. Mater. Electron.* **31** 3729–3749 (2020)
3. F. J. Serrao et al., *J. Optoelectron. Adv. Mater.* **18** 672–678 (2016)
4. P. Sengunthar et al., *Appl. Phys. A Mater. Sci. Process.***126** 1–9 (2020)
5. F. J. Serrao et al., *Appl. Phys. A Mater. Sci. Process.* **124** 1–7 (2018)
6. W. H. Nam et al., *Appl. Sci.***10** 1–8 (2020)
7. V. S. Kindalkar et al., *Mater. Res. Express* **6** (2019)
8. S. Safa et al., *Phys. E Low-Dimensional Syst. Nanostructures* **57** 155–160 (2014)

Estimation of ^{55}Fe reaction cross-section from threshold to 20 MeV

Rita Crasta[1*], Anagha V Nair[1], Namitha C P K[1], Paresh Prajapathi[2]

[1]*Department of Postgraduate Studies and Research in Physics, St Aloysius (Deemed to be University), Mangalore, 575003*

[2]*Manipal Centre for Natural Sciences, Manipal, Karnataka, 576104*

*E-mail: rita_crasta@staloysius.edu.in

Abstract

The determination of nuclear cross-section data for reactions involving the (n, p), (n, α), (n, d), and (n, γ), channels on a ^{55}Fe target is crucial for advancing future applications in fusion energy. To achieve this, the nuclear reaction model code TALYS-1.96 has been employed to calculate the cross-sections for these reactions over the energy range from threshold to 20 MeV. These computed results have been compared with existing nuclear data libraries, including ENDF/B-VIII.0, TENDL-5, ROSFOND-2010, JENDL-5, and JEFF-3.3. The study revealed that the accurate cross-section measurements for these ^{55}Fe target reactions are expected to improve radioactive waste management in fusion reactors.

Keywords: TALYS-1.96, nuclear data libraries, Excitation function

1 Introduction

Nuclear energy is a strong power source used widely for making electricity, exploring space, medical tests, agriculture, and more. Nuclear power facilities are built and run to generate these large amounts of electricity. Since the fusion program is currently focused on designing the test blanket module (TBM), certain elements namely Be, Pb, Li, Si, O, Fe, Cr, W, Ta, Cu, and Ti are given high priority [1]. Reliable data, especially on their natural isotope reactions, is needed. Stainless steel, which plays an important role in the structure of fusion reactors, is made from Fe, Ni, Cr, Mn, Co and Nb, with Fe being the main element**.**

During nuclear fusion, high-energy neutrons are produced in the reactor and strike reactor walls. This leads to the creation of large amounts of the radioisotope ^{55}Fe, which has a half-life of 2.73 years. It is formed through various reactions, such as ^{58}Ni(n, α), ^{54}Fe(n, γ), and ^{56}Fe(n, 2n). ^{55}Fe, a radioactive form of iron, is mostly produced inside fusion reactors and triggers reactions like (n, p), (n, α), (n, d), and (n, γ) which result in the creation of hydrogen, helium, deuterium gases and gamma. The production of these gases can severely damage the reactor's structural materials,

leading to bulging and failure of the first wall before the main structural components [2]. Therefore, accurate cross-sectional data on neutron-induced reactions are essential for fusion reactor design. As a result, nuclear data libraries must include cross-section data for unstable radionuclides or radioactive materials.

This study aims to investigate the excitation function of neutron-induced reactions on ^{55}Fe in the energy range from threshold to 20 MeV, which is critical for fusion reactor technology, particularly concerning the production of helium, hydrogen, deuterium, and gamma radiation. To achieve this, the excitation function for various reactions on ^{55}Fe has been calculated using the TALYS-1.96 code [3] and compared with the latest nuclear data libraries ENDF/B-VIII.0 [4], TENDL-5 [5], ROSFOND-2010 [6], JENDL-5 [7], and JEFF-3.3 [8].

2 Nuclear Model Calculations

The TALYS-1.96 nuclear reaction code was used to calculate the excitation function for ^{55}Fe. This code serves two primary functions: it acts as a nuclear physics tool to validate nuclear models against experimental data and a nuclear data tool to predict nuclear properties when experimental data are unavailable. In this study, the excitation functions for ^{55}Fe were calculated for different channels, including (n, p), (n, α), (n, d), and (n, γ), reactions, from their respective thresholds up to 20 MeV using TALYS-1.96. TALYS is a nuclear reaction computer program used to analyze nuclear reactions for target nuclides of masses 12 and above. The main objective is to simulate nuclear processes including neutrons, photons, ^{1}H, ^{2}H, ^{3}H, ^{3}He, and α-particles in the energy range of eV to 200 MeV.

3 Results and Discussion

The nuclear reaction model code TALYS 1.96 is used to determine the cross-sections (n, p), (n, α), (n, d), and (n, γ), reactions on the ^{55}Fe target from threshold to 20 MeV. The acquired cross-section from TALYs has been compared with the latest available nuclear data libraries like ENDF/B-VIII.0, TENDL-5, ROSFOND-2010, JENDL-5, and JEFF-3.3. Figures 1 through 4 present the results of the nuclear model calculations along with nuclear data from various libraries.

It can be seen in Figure 1 that, at lower energies, the incident neutron and outgoing proton have a higher probability of forming a Compound nucleus due to longer interaction times. The specific energy of the incident neutron can influence the probability of forming this compound nucleus with certain configurations. Protons and neutrons are subjected to a strong nuclear force, at higher energies, the neutron is more likely to overcome the potential barrier and pass through the target proton without interacting.

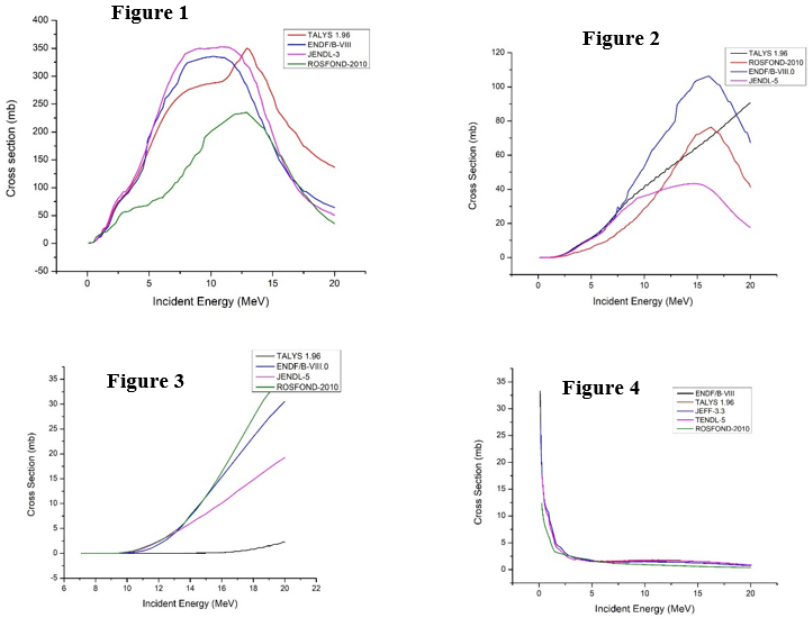

Fig. 1 to 4: Comparison of calculated excitation functions of ^{55}Fe (n, p), ^{55}Fe (n, α), ^{55}Fe (n, d), and ^{55}Fe (n, γ) with evaluated nuclear data files

The formation of the compound nucleus can be through a series of resonances, where specific energy levels of a combined system offer a higher probability of interaction. At even higher energies, the incident neutron might still interact with the target proton, but instead of forming a compound nucleus, it might directly scatter off the proton or cause other reactions.

The ^{55}Fe (n, α), reaction cross-section plot is represented in Figure 2. At lower energies, the incident particle encounters a significant repulsive force from the positively charged target nucleus. Only particles with sufficient kinetic energy can overcome this Coulomb barrier and approach the nucleus, resulting in a low reaction cross-section at lower energies. Once the Coulomb barrier is surpassed, the probability of a reaction increases as the nuclei can interact, potentially forming a temporary compound nucleus. The stability and lifetime of this compound nucleus are governed by its internal energy levels. At specific incident particle energies, the energy may resonate with these internal levels, significantly enhancing the reaction probability and creating a peak in the reaction cross-section. As the particle energy rises beyond the resonance peak, other reaction channels become energetically accessible, such as the breakup of the incident or target nucleus or the emission of additional particles.

It is observed from Figure 3 that, at lower neutron energies, the ^{55}Fe (n, α), cross-section is less due to the lack of incident neutron energy to overcome the Coulomb barrier and to cause deuteron emission. As neutron energy increases gradually, the reaction becomes more probable. At higher energies, it overcomes the Coulomb barrier and hence, the cross-section also increases. At very high energies the other reaction channels will open up. Figure 4 shows the cross-section for the ^{55}Fe (n, γ) reaction. It can be seen that at lower energies the neutron capture is greater. Therefore, the cross-section is also higher. As neutron energy increases, resonance peaks are observed due to the greater capture of neutrons. Beyond this region, the cross-section decreases as the increase of neutron energy.

4 Conclusions

The excitation function for ^{55}Fe(n, p), ^{55}Fe(n, α), ^{55}Fe(n, d), and ^{55}Fe(n, γ) reactions was calculated from threshold to 20 MeV neutron energy using TALYS 1.96 nuclear model code. These cross-section values are compared with the latest nuclear data libraries. The results obtained from TALYS are in good agreement with nuclear data libraries. In the absence of experimental data, TALYS provides a way to calculate the excitation function.

References

1. U. Fischer et al., *AIP Conf. Proc.* **769** 1478 (2005)
2. P. M. Prajapati et al., *Fusion Science & Technology* **66**(3) 426–431 (2014)
3. A. J. Koning et al., TALYS User Manual, A Nuclear Reaction Program, NRG-1755 ZG Petten, NRG Petten, 2011
4. M. B. Chadwick et al., *Nucl. Data Sheets* **112** 2887 (2011)
5. A. J. Koning, Nuclear Research and Consultancy Group, NRG, Petten, 2012
6. ROSFOND-2010: Updated Russian Library of Evaluated Neutron Data, Jan. 18, 2014
7. K. Shibata et al., *J. Nucl. Sci. Technol.* **48** 1 (2011)
8. A. J. Koning et al., *Proc. Int. Conf. Nuclear Data for Science and Technology,* Nice, France, 2007, EDP Sciences (2008)

Assessment of Radon Concentration in Groundwater using Emanometry Techniques: A Study in Dakshina Kannada District

Rishika[1], Greeshma K V[1], Rita Crasta[1*], Suresh S[2]
[1]*Department of Postgraduate Studies and Research in Physics, St Aloysius (Deemed to be University), Mangalore, 575003*
[2]*Department of Physics, M.P.E Society's S.D.M Degree College, Honnavar, 581334*

*E-mail: rita_crasta@staloysius.edu.in

Abstract

Radon, a naturally occurring radioactive gas found in groundwater, poses significant health risks. Therefore, monitoring its levels is essential for assessing potential hazards and implementing effective mitigation measures. In the present work, ^{222}Rn concentrations were measured in groundwater samples from different regions of Dakshina Kannada district. Using Radon bubbler and Emanometry techniques with Luca's cells, the study determined that radon activity levels ranged from 1.40 Bq/L to 12.44 Bq/L, averaging 3.93 Bq/L. Importantly, all measured radon levels were below the World Health Organization's (WHO) recommended reference value of 100 Bq/L. The annual effective dose due to radon activity in groundwater varied between 3.83 µSv/year and 29.67 µSv/year, with an average of 10.80 µSv/year. This average annual dose is well below the WHO's safety limit of 100 µSv/year, highlighting a low health risk associated with radon exposure in the study area.

Keywords: Emanometry, Radon bubbler, Total effective dose, Ingestion, and inhalation.

1 Introduction

Radon-222 (^{222}Rn), a decay product of uranium and thorium, is a major contributor to natural radiation, primarily affecting human exposure through its accumulation in enclosed spaces like buildings and underground mines. The concentration of radon in groundwater is influenced by geological factors such as soil types, rock formations, and hydrogeological conditions. This radioactive gas, with a half-life of 3.8 days, can seep into groundwater, increasing its radioactivity. When radon-contaminated water is consumed, it exposes the gastrointestinal tract to radiation, and when radon escapes into indoor air, it can be inhaled, posing risks such as lung and liver cancer [1].

This study focuses on the Dakshina Kannada district in Karnataka, India, characterized by the Western Ghats, granite formations, and laterite soils, which may influence natural radon emissions. The aim is to assess whether radon levels in the region's

groundwater fall within the safety limits set by the World Health Organization and other scientific bodies.

2 Materials and Methods/Model

Sample collection

Eighty water samples were collected from four regions in Dakshina Kannada: Mulki, Moodabire, Konaje, and Panambur, chosen for their diverse geography. Twenty samples from each region were gathered, following standard protocols to prevent radon out-gassing. The samples were sealed underwater and transported to the lab within 24 hours for radon-222 analysis [2].

Measurement of ^{222}Rn concentration and Assessment of equivalent effective dose

Radon concentrations were measured using emanometric techniques. 70 ml of water was transferred to a bubbler and the radon was moved into a pre-evacuated scintillation cell. After reaching equilibrium, alpha particles were counted. The ^{222}Rn activity concentration A_w (Bq/l) in groundwater was calculated using the equation:

$$A_w = \frac{6.97\times10^{-2}\times D}{V\times E\times(e^{-\lambda t})(1-e^{-\lambda t})} \quad (1)$$

where D is the counts above the background, V volume of water, E efficiency of the scintillation cell (75%), λ decay constant of radon, T is the counting delay after the sampling and t is the counting duration.

Radon exposure occurs via inhalation and ingestion. The effective inhalation dose E_{in} (μSv/y) is estimated using:

$$E_{in}\,(\mu Svy^{-1}) = C_{Rn}\times R_{aw}\times I\times O\times K \quad (2)$$

C_{Rn} is the ^{222}Rn concentration in water in Bql^{-1}, R_{aw} is the air-to-water radon ratio, I is the equilibrium factor between radon and its progenies, O is the average indoor occupancy time per individual, and K is the dose conversion factor for radon exposure. The ingestion dosage E_{ing} is calculated as,

$$E_{ing}\,(\mu Svy^{-1}) = C_{Rn}\times A_w\times D \quad (3)$$

A_w is the water consumption, and D is the ingestion dose coefficient [3].

The sum of annual effective doses for inhalation and ingestion is calculated for each water sample, representing the total annual effective dose of radon exposure to humans.

3 Results and Discussions

This study analyzes Rn-222 levels in water samples from Mulky, Moodabidre, Panambur, and Konaje regions of Dakshina Kannada district using emanometry. The

results, summarized in Table 1, and are compared with drinking water standards.

Table 1: Radon concentration and dosage exposure levels in water samples

Location		Rn Concentration (Bq/L)	Inhalation Dose (µSv/y)	Ingestion Dose (µSv/y)	Total Effective Dose (µSv/y)
Mulky	Max	7.78	19.62	1.63	21.25
	Min	1.40	3.54	0.29	3.83
	Mean	3.32	8.65	0.72	9.37
Moodabidre	Max	12.44	31.35	2.61	33.96
	Min	1.93	4.87	0.41	5.27
	Mean	5.03	12.68	1.06	13.74
Konaje	Max	10.87	27.39	1.86	29.67
	Min	1.79	4.51	0.32	4.89
	Mean	4.88	12.30	1.02	13.32
Panambur	Max	4.80	12.10	1.01	13.11
	Min	1.49	3.75	0.31	4.06
	Mean	2.48	6.25	0.52	6.77
Total Variations	Max	12.44	27.39	1.86	29.67
	Min	1.40	3.54	0.29	3.83
	Average	3.93	9.97	0.83	10.80

It is observed from Table 1 that, the radon concentration levels varied due to rock distribution and sampling depth, with Moodabidre showing the highest concentrations, likely due to deeper water sources in hilly areas, while coastal regions like Mulky and Panambur had lower levels. Elevated radon levels are linked to geological factors, such as radioactive elements in granite and local geological features [2].

The ^{222}Rn dosage exposure levels with different ^{222}Rn concentrations is shown in Figure 1. The analysis reveals a strong correlation between radon concentration and exposure dosage, as depicted in Figure 1, with inhalation being the primary contributor to the total effective dose. The total dose ranges from 3.83 to 29.67 µSv/y, with an average of 10.80 µSv/y.

4 Conclusions

The study measured radon concentrations in water samples from Mulky, Moodabidre, Panambur, and Konaje in Dakshina Kannada District using the emanometry technique. All samples had radon levels below the WHO's safe limit of 100 Bq/l, and the exposure doses were within the 100 µSv/y action value. Thus, the water in these locations is safe for consumption.

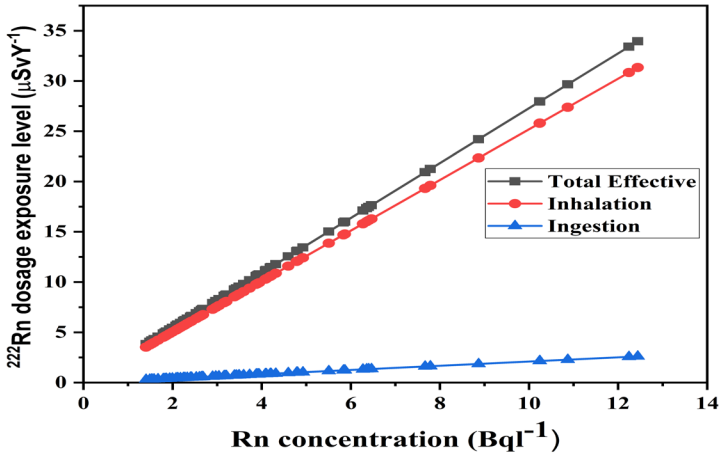

Fig. 1 Plot depicting the ^{222}Rn dosage exposure levels with different ^{222}Rn concentrations

Acknowledgements

The authors thank the Mangalore Jesuit Educational Society (MJES), St Aloysius College (Autonomous), Mangalore for their generous seed grant. The authors would like to sincerely thank Dr M.P. Karki Institute of Excellence and Research, Honnavar for providing an instrumentation facility to carry out the research work.

References

1. P. Vipin Kumar, et al., *Radiation Protection Dosimetry* **183**(4) 514-521 (2019)
2. M. C. Srilatha, D. R. Rangaswamy, J. Sannappa, *Int J Adv Sci Tech Res* **2**(4) 641-660 (2014)
3. P. V. Divya, V. Prakash, *Radiation Protection and Environment* **41**(2) 84-87 (2018)

Influence of GO Incorporation on the Structural, Electrical and Mechanical Properties of Chitosan/Methylcellulose Polymer Blend Thin films

Shilpa Thomas*[1], Rashmi N[2], Felcy Jyothi Serrao[2], Kumara K[3]
[1]*Department of PG Studies and Research in Physics, St. Aloysius (Deemed to be University), Mangalore 575003, India*
[2]*Department of Physics, Sahyadri College of Engineering & Management (Autonomous), Mangaluru 575007, India*
[3]*Department of Physics, M.P.E Society's S.D.M. Degree College, Honnavar, 581334, India*

* E-mail: shilpathomas021@gmail.com

Abstract

Polymer blends are increasingly vital for developing advanced, cost-effective, and sustainable materials. This study explores the impact of Graphene Oxide (GO) on the structural, electrical, and mechanical properties of chitosan/methylcellulose (CS/MC) polymer blend thin films. X-ray diffraction (XRD), Fourier-transform infrared (FTIR), Electrical impedance spectroscopy (EIS) and Mechanical tests are used to investigate structural, chemical, electrical and mechanical properties of the polymer blend thin films.

Key words: Polymer blend, Polymer, Graphene Oxide, Conductivity, Young's Modulus

1. Introduction

The pursuit of advanced materials with enhanced properties has spurred significant research into polymer blends and composites, which offer the potential to combine the best attributes of different polymers. Among these, the Chitosan/Methylcellulose (CS/MC) polymer blend stands out due to its promising applications in areas such as biodegradable packaging, tissue engineering, and environmental remediation [1]. Both Chitosan, a natural polymer derived from chitin, and Methylcellulose, a cellulose derivative, are valued for their biocompatibility, film-forming capabilities, and environmental friendliness [2]. However, to further expand the applicability and performance of CS/MC blends, researchers are turning to the incorporation of nanomaterials to modify and enhance their properties. Graphene oxide (GO), known for its remarkable electrical conductivity, high surface area, and mechanical strength, presents a particularly intriguing opportunity [3]. The addition of GO into the Ch/Mc polymer matrix could potentially improve the structural stability, electrical conductivity, and mechanical strength of the resulting thin films [4-5]. This study investigates the impact of GO incorporation on the structural, electrical, and

mechanical properties of Chitosan/Methylcellulose polymer blend thin films. By systematically evaluating these properties, we aim to determine how GO modifies the intrinsic characteristics of the CS/MC blend and to assess the potential benefits and trade-offs associated with its incorporation.

2. Synthesis of Chitosan/Methylcellulose/GO thin films

Chitosan (1.4 g) and methylcellulose (0.6 g) were dissolved in 1% acetic acid solution (prepared from 1 ml glacial acetic acid in 99 ml distilled water) by stirring at 50°C for 7-8 hours. The polymer blend was then poured into a Petri dish and dried at 40°C for 72 hours. For Chitosan/Methylcellulose/GO thin films, 0.02-0.06 g of GO was sonicated in 10 ml distilled water for 1 hour, then added to the polymer mixture and stirred overnight. The final blend was poured into a Petri dish and dried at 40°C overnight.

3. Results and Discussion

The XRD patterns of thin films as shown in the figure 1. Pure CS exhibits crystalline peaks at 2θ = 15.1°, 17.7°, and 20.9° [6-7]. According to reports, there is just one hollow in MC material at 2θ = 8.5°, 19–21° [8-9]. Interestingly, the CS/MC matrix's hollow intensity was dramatically reduced with the addition of GO. This may serve as proof that the crystalline portion of the CS matrix is shrinking. The XRD pattern makes it clear that adding more GO to the CS/MC combination can cause the hollow to become more pronounced. It is clear that the amorphous region within the blended polymer body is dominating from the peak broadening and intensity decrease [7]. The peak for GO vanished, indicating good dispersion of nanofillers. Blending MC with CS reduces CS's crystallinity due to interactions and disrupted hydrogen bonds. The peak at 2θ = 8° shows MC's tri-methyl glucose units. Increasing GO concentration in the composite enhances peak intensity at 2θ = 8°, likely due to improved crystallinity, reinforcement, and interfacial interactions. Greater peak broadness suggests an increase in the amorphous content. Figure 2 shows the FTIR spectra of the thin films.

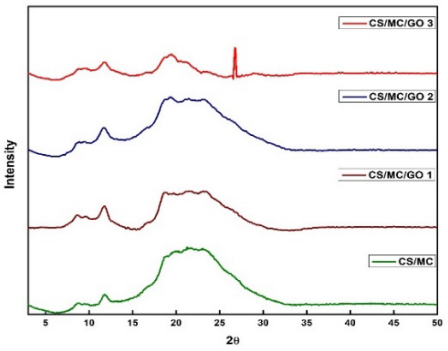

Fig 1 XRD pattern of the thin films

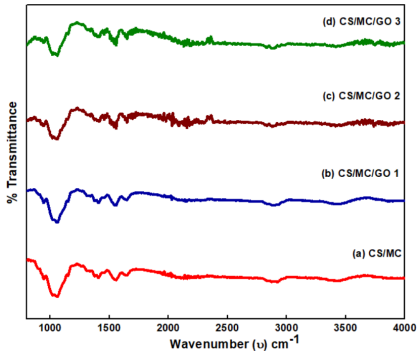

Fig 2 FTIR spectra of the Thin films

Table 1: FTIR Peak details of polymer blend

Band Assignment	Wavenumber (cm^{-1})			
	CS/MC	CS/MC/GO 1	CS/MC/GO 2	CS/MC/GO 3
C-O bending	1060	1058	1057	1063
C-O stretching	1020	1020	1016	1020
N-H bending	1559	1557	1544	1559
C=O stretching	1651	1651	1646	1650
C-H stretching	2922	2891	2870	2892
-OH stretching	3450	3436	3421	3432

The addition of graphene oxide enhances this hydrogen bonding and decreases the intensity of the chitosan and methylcellulose peaks. Table 1 shows the peak details of polymer blend thin films.

Electrical impedance spectroscopy (EIS) indicated that GO significantly enhanced ionic conductivity, with a maximum conductivity of 8.28×10^{-6} S/cm observed at 1 wt% GO (Figure 3). The conductivity details of all thin films are listed in Table 2.

Mechanical properties are crucial for determining the applications of polymer blend thin films. Stress-strain curves for pure CS/MC and GO-incorporated CS/MC films is shown in figure 4. The inclusion of Graphene Oxide (GO) significantly improves the mechanical properties of the CS/MC blend, increasing both stiffness (Young's modulus) and tensile strength. Table 2 gives the details of Young's modulus and tensile strength of thin films. The enhanced stiffness results from GO's high aspect ratio, surface area, and strong interaction with the polymer matrix, which restricts polymer chain mobility. The increase in tensile strength indicates improved load-bearing capacity, highlighting GO's role as an effective reinforcing agent.

Table 2: Ionic conductivty, Young's modulus and tensile strnegth of thin films

Sample	Weight % of GO	Ionic conductivity S/cm	Young's Modulus	Tensile Strength
CS/MC	0	$1.19 * 10^{-6}$	229.8	23
CS/MC/GO 1	1	$8.28 * 10^{-6}$	372.7	27.1
CS/MC/GO 2	2	$4.53 * 10^{-6}$	439.8	27.8
CS/MC/GO 3	3	$6.51 * 10^{-6}$	496.7	32.6

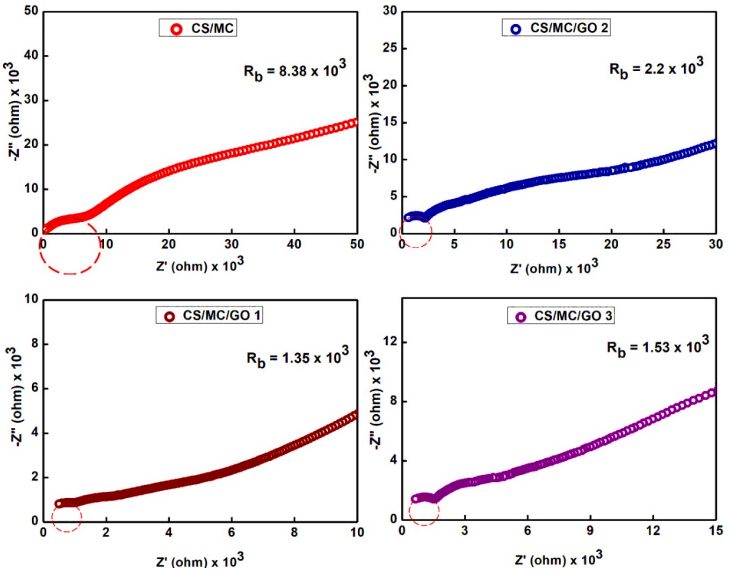

Fig. 3 Electrical impedance spectra of thin films

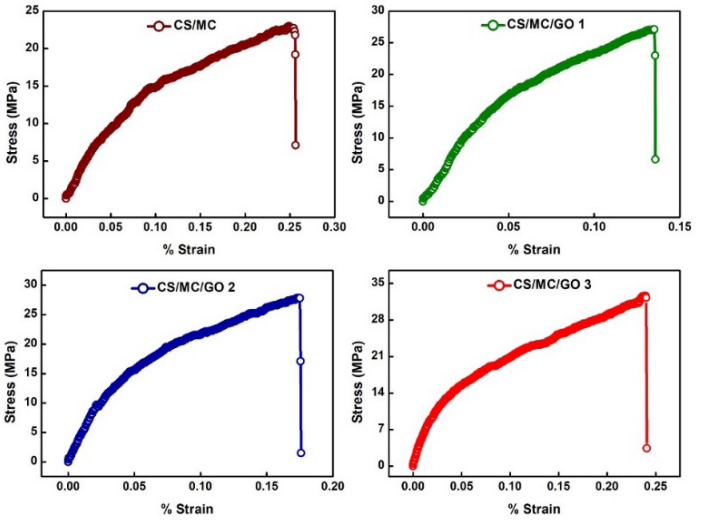

Fig. 4 The stress-strain curves of thin films

Conclusion

In conclusion, XRD analysis demonstrates that the incorporation of Graphene Oxide (GO) into Chitosan (CS)/Methylcellulose (MC) blends reduces the crystallinity of CS, enhancing the blend's amorphous nature and improving interfacial interactions, as indicated by the changes in peak intensity and broadening. FTIR spectroscopy

confirms successful polymer blending and increased hydrogen bonding with the addition of GO. Electrical impedance spectroscopy shows that GO significantly boosts ionic conductivity, with a peak conductivity of 8.28×10^{-6} S/cm at 1 wt% GO. Mechanical testing reveals that GO enhances both stiffness (Young's modulus) and tensile strength, making the composite more load-bearing and reinforcing its potential applications. The results underscore GO's effectiveness in improving the performance of polymer blend thin films, with further optimization needed to balance strength and ductility for specific applications.

References

1. Rinaudo, M, *Progress in Polymer Science* **31**, 603-632 (2006).
2. Williams, C. K., & Hillmyer, M. A, *Polymer* **49**, 1333-1343 (2008).
3. Gopinath, S. C. B., & Zhang, S, *Biotechnology Advances* **32**, 328-338 (2014).
4. Wang, H., & Chen, S, *Chem. Soci. Rev.* **41**, 4862-4880 (2012).
5. Kuila, T., Bose, S., Khan, Y., Kim, N. H., & Lee, J. H. *Prog. in Pol. Sci.* **37**, 1061-1105 (2012).
6. S. B. Aziz, M. F. Z. Kadir, and Z. H. Z. Abidin, *Int J Electrochem Sci*. **11,** 9228–9244 (2016).
7. S. B. Aziz, Z. H. Z. Abidin, and M. F. Z. Kadir, *Phys Scr*. **90**, 3 (2015).
8. S. B. Aziz, M. A. Rasheed, and H. M. Ahmed, *Polymers (Basel)*, **9,** (2017).
9. N. A. Nik Aziz, N. K. Idris, and M. I. N. Isa, *J. Apply. Poly. Sci*. **15** 319–327 (2010).

Growth and Characterisation of a (2E)-3-(4-iodophenyl)-1-(4-nitrophenyl) prop-2-en-1-one for Nonlinear Optical Applications

P. Gayathri, Maringmei Linda, T. Chandra Shekhara Shetty*
Department of Physics, St Aloysius (Deemed to be University) Mangaluru-India-575 003.

*Email: tcsshetty@gmail.com

Abstract

A new chalcone derivative (2E)-3-(4-iodophenyl)-1-(4-nitrophenyl) prop-2-en-1-one (4I4N) crystal has been grown by a slow evaporation solution growth technique at room temperature. The crystalline powder of the grown crystal was examined by X-ray powder diffraction and result shows the compound's purity and crystallinity. By using FT-IR spectral analysis the different functional groups contained in the crystal was identified, and found that the crystal is highly transparent over the whole visible and infrared spectrum. The cut-off wavelength of the crystal is proven to be 456.6 nm by UV-Visible spectroscopy. A single beam Z-scan method was utilised to determine the nonlinear absorption coefficient, which is found to be $11\times10^{-7} cmW^{-1}$ *for an irradiation of* $1.81 \times10^{8} Wm^{2}$*. The crystal 4I4N exhibit efficient nonlinear optical properties.*

Key words: Chalcones; Z-scan; nonlinear optical

1 Introduction

Nonlinear optical Materials play important role in applications such as optical data storage, optical switching, and optical communication in the recent years [1-3]. Among all types of NLO materials, organic molecules have attracted researchers recently due to their large optical susceptibility, greater laser damage threshold, ultrafast response time, and tailor-ability of the designed molecule. When these molecules are grown into crystals, the third-order nonlinear optical properties of these molecules will be useful in optical communications, photonics, optical limiting, and optical data storage applications [4-7]. The delocalized π-electron system and molecular interaction leading to a strong donor-acceptor mechanism in these molecules are responsible for the NLO effects. Two planar rings connected through a conjugated double bond present in chalcones (α,β-unsaturated ketones) act like a platform for this type of activity leading to third-order nonlinear optical (TNLO) properties [8]. Many researchers fine-tuned the NLO properties of chalcones by substituting suitable donor-accepter groups. The properties such as optical limiting (OL), reverse saturable

absorption (RSA), nonlinear refraction (NLR), nonlinear optical absorption (NLA), etc [9]. We synthesized an efficient chalcone derivative showing TNLO efficiency.

2 Materials and Methods/Model

2.1 Synthesis

The Claisen-Schmidt condensation process was used to prepare the novel chalcone derivatives. The reactants from Sigma Aldrich 4′-Iodoacetophenone (0.01 ml) and 4′-Nitrobenzaldhehyde(0.01 ml) were dissolved in 40 ml of ethanol and stirred rigorously for three hours in alkaline medium (5% NaOH) in a constant temperature 32℃ during the entire process. The acquired products were filtered, dried, washed and kept for recrystallization to obtain 2E)-3-(4-iodophenyl)-1-(4-nitrophenyl) prop-2-en-1-one (4I4N). The Synthesis scheme is shown in the fig.1.

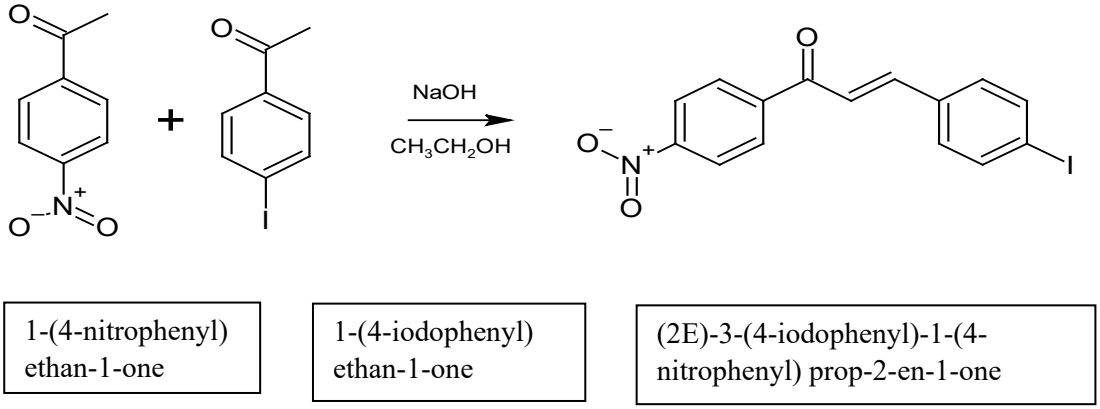

Fig. 1 Synthesis Scheme of the compound 4I4N

2.2 Crystal growth

The single crystal of 4I4N was grown using solution growth approach using acetone as the solvent. The high-quality clear single crystals of considerable size were observed after five to seven days.

3 Results and Discussions

3.1 XRD Analysis

The newly grown crystals was coarsely pulverized and sent through a Rigaku MiniFlex XRD powder XRD examination. The XRD profiles demonstrate that the sample is single phase and devoid of any discernible impurities (Fig. 2). The well-defined Bragg's peaks at particular 2θ angles indicate a high degree of crystallinity in the substance.

3.2 UV-Visible spectroscopy

A Cary 60-Agilent high resolution spectrophotometer was used to record the formed crystals' UV-Vis spectrum, covering the wavelength range of 200-1000 nm. We deduce that the crystal's absorption cut off wavelength of 456.6 nm can be ascribed to n→π* and may be related to the aromatic ring and C=O group excitation. There are no absorption peaks above this range that reach the infrared spectrum. This crystal's broad transparency range might make it useful for nonlinear optical applications.

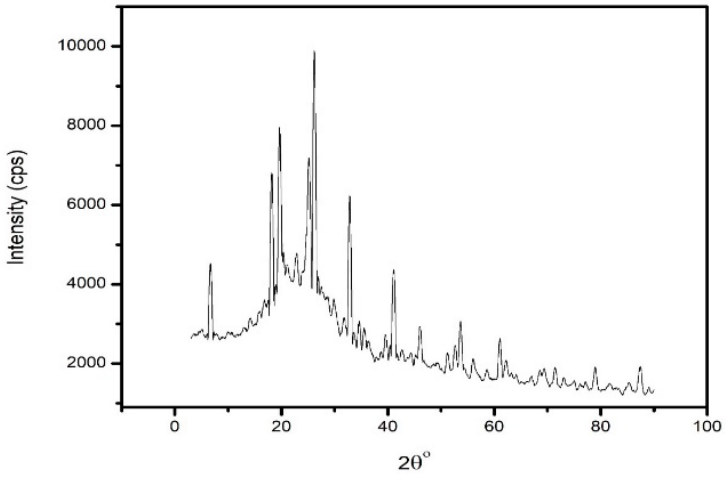

Fig. 2 Powder XRD Pattern of 4I4N

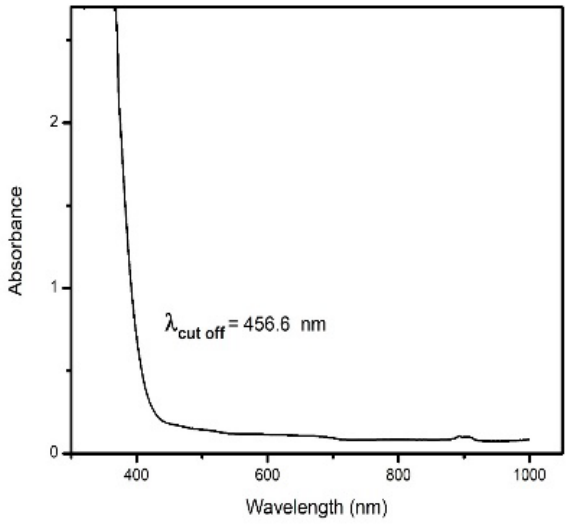

Fig. 3 (a) Absorption Spectrum of 4I4N

3.3 FT-IR Analysis

The FTIR spectrum of $C_{15}H_{10}N_1O_3I_1$ was recorded between 400 to 4000 cm^{-1} using Perkin Elmer Spectrometer. FTIR spectra affirmed the presence of varied functional groups, and distinctive peaks were identified by comparing them with the chalcone derivative's conventional FT-IR pattern. The FT-IR spectrum of the title compound is shown in the fig. 4.

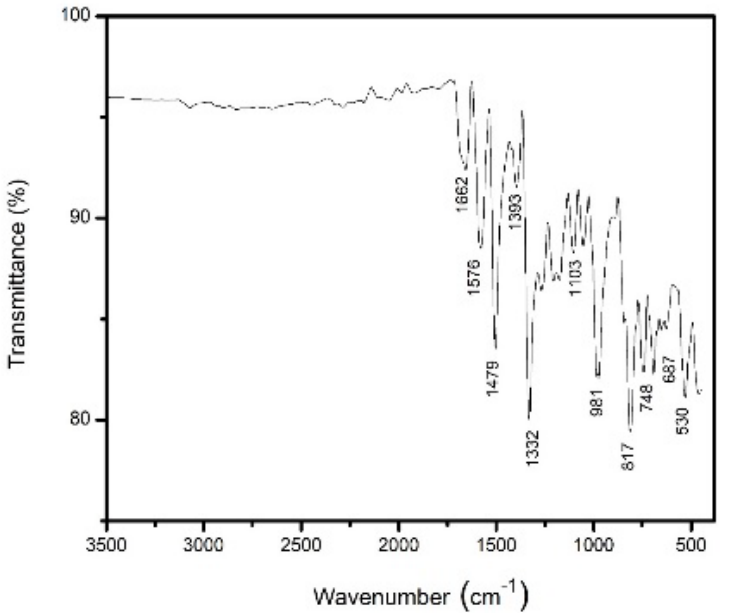

Fig. 4 FT-IR Spectrum of 4I4N

3.4 Nonlinear Optical Properties

The third-order non-linear absorption (NLA) and non-linear refraction (NLR) of the novel chalcone was investigated concurrently using a single-beam z-scan approach. Z-scan open apertures (OA) is performed to estimate the non-linear absorption coefficient (ß). Conforming the data from the experiment to the theoretical open-aperture Z-scan transmittance equation yields the nonlinear absorption coefficient (β_{eff}):

$$T(z) = 1 - \left(\frac{1}{2\sqrt{2}} \beta_{eff} I_0 L_{eff} \left[\frac{1}{1 + \frac{z^2}{z_0^2}} \right] \right)$$

This equation denotes the following:

$z_0 = \frac{\pi \omega_0^2}{\lambda}$ is the sample's Rayleigh length; I_0 is the on-axis peak irradiance at focus;

$L_{eff} = \frac{[1-e^{-\alpha L}]}{\alpha}$ is the solution's effective thickness and α is the linear absorption coefficient: and β_{eff} is the nonlinear absorption coefficient. Fig. 5 shows that the NLA increases as input intensity increases, meaning that the depth of the valley increases as irradiance. The non-linear absorption coefficient for an input irradiance of 1.8×10^8 Wm^2 is observed to be 11×10^{-7} cmW^{-1} .

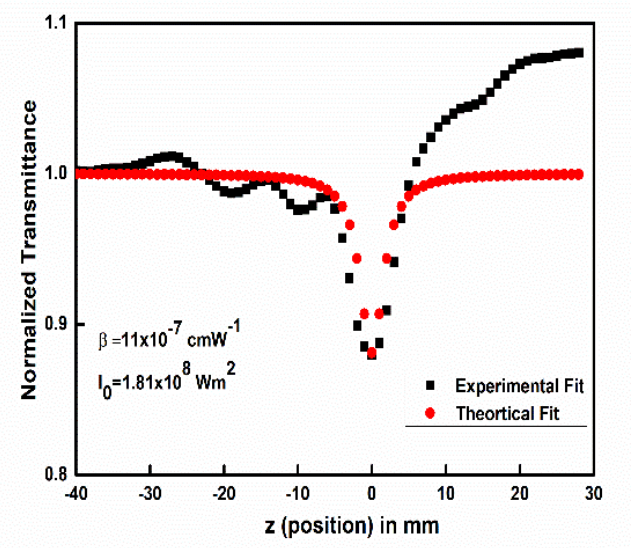

Fig. 5 Open aperture Z-scan Curve of 4I4N

4 Conclusion

The new chalcone derivative was grown by means of solution growth technique (2E)-3-(4-iodophenyl)-1-(4-nitrophenyl) prop-2-en-1-one crystal at room temperature. Powder XRD result shows the compound's purity and crystallinity. By using FT-IR spectral analysis the different functional groups contained in the crystal was identified, and found that the crystal is highly transparent over the whole visible and infrared spectrum. The cut off wavelength of the crystal is proven to be 456.6 nm. A single beam Z-scan method was utilised to nonlinear absorption coefficient. The formed crystal exhibit nonlinear optical properties.

Acknowledgements

Authors acknowledge the support provided by the Coordinator DST-FIST of St Aloysius College (Autonomous) for providing experimental facilities.

References

1. S. Tao, T. Miyagoe, A. Maeda, H. Matsuzaki, H. Ohtsu, M. Hasegawa, et al., *Adv. Mater.* **19** 2707 (2007)
2. I. Polyzos, G. Tsigaridas, M. Fakis, V. Giannetas, P. Persephonis, J. Mikroyannidis, *Chem. Phys. Lett.* **369** 264 (2003)
3. K. Naseema, V. Rao, K.B. Manjunatha, G. Umesh, K.V. Sujith, B. Kalluraya, *J. Opt.* **39** 143 (2010)
4. E. D. D, D. N. Rao, R. Philip, R. J. Butcher, S. M. Dharmaprakash, *Phys. B Phys. Condens. Matter.* **406** 2206–2210 (2011)
5. J. Indira, P. P. Karat, B. K. Sarojini, *J. of Cryt. Growth*, **242** 209–214 (2002)
6. S. Hu, T. Zhao, K. Xu, S. Ji, L. Cao, B. Teng, *Optik* **231** 166410 (2021)
7. K. B. Manjunatha, R. Dileep, G. Umesh, M. N. Satyanarayan, B. Ramachandra Bhat, *Opt. Mater. (Amst).* **36** 1054–1059 (2014)
8. K. Naseema, K. V. Sujith, K. B. Manjunatha, B. Kalluraya, G. Umesh, V. Rao, *Opt. Laser Technol.* **42** 741–748 (2010)
9. V. Kumari, Int. J. Pure Appl. Phys. **14** 125 (2018)

ADVISORY COMMITTEE

Rev. Dr Praveen Martis SJ	-	Vice Chancellor
Dr Ronald Nazareth	-	Registrar
Rev. Fr Vishwas Misquith SJ	-	Finance Officer
Prof. S.M. Dharmaprakash	-	Formerly Professor, Dept. of Physics, Mangalore University
Prof. Jagannatha N.	-	Dept. of Physics, University College, Mangaluru
Prof. Arumugam Thamizhavel	-	Professor, Dept of Condensed Matter Physics & Materials Science, TIFR, Mumbai
Prof. B. R. Shankar	-	Dept of MACS, NITK, Surathkal
Prof. Prakash P. Karat	-	Formerly Professor, Dept of PG Physics
Prof. Y. Sangappa	-	Chairman, Dept of Physics, Mangalore University
Dr Asha Abraham	-	Director, LCRI Block
Dr Aruna Kalkur	-	Dean, School of Physical Sciences
Mr Naveen P. Mascarenhas	-	Chair, Student Engagements (Ext.)
Dr Kumara K.	-	Dept of Physics, SDM College, Honnavar

ORGANIZING COMMITTEE

Dr Chandra Shekhara Shetty	-	Dept. of Physics (PG),Convener
Ms Anupriya Shetty	-	Dept. of Mathematics (PG) Co-Convener
Dr E. Deepak Dsilva	-	Dept. of Physics (PG) Organising Secretary
Dr. Ishwara Bhat	-	HOD, Dept. of Physics
Dr Nilakanthan V.K.	-	Dept. of Physics (PG)
Dr Rita Crasta	-	Dept. of Physics (PG)
Dr D. Shubhalakshmi	-	Dept. of Mathematics (PG)
Mr Chriswin Vas	-	Dept. of Mathematics (PG)
Dr Praveen Prakash D Souza	-	Dept. of Physics (PG)
Ms Sweety Basil	-	Dept. of Mathematics (PG)

KEY SPEAKERS
AT THE NATIONAL CONFERENCE

Dr Shaikh Faruque Ali
Professor, Department of Applied Mechanics
IIT Madras

Dr Praveen C Ramamurthy
Professor, Department of Materials Engeneering,
Indian Institute of Science, Bengaluru

Dr Nagesh S Kini
Co-Founder & Chief Technology Officer,
Vimano EWA Pvt. Ltd. Bengaluru

Dr Vasudha Hegde
Professor, Department of Electrical
& Electronics Engineering, Nitte Meenakshi
Institute of Technology, Bengaluru

Dr Anindita Roy
Associate Professor, Department of Mechanical
Engineering, Symbiosis Institute of
Technology, Maharashtra

K. S. Narayan
Professor, Jawaharlal Nehru Centre
for Advanced Scientific Research,
(JNCASR), Jakkur, Bangalore

Dr P.M. Aneesh
Assistant Professor, Department of Physics, Central University of Kerala

EHT-TPN 2024

Sponsored by

Science and Engineering Research Board(SERB)
Department of Science and Technology (DST)
Govt. of India

Supported by

Mangalore Refinery and Petrochemicals Limited

978-81-963171-6-4

₹150.00